

Published in final edited form as:

Prog Mater Sci. 2014 October 1; 66: 87–111. doi:10.1016/j.pmatsci.2014.06.001.

Piezoelectric single crystals for ultrasonic transducers in biomedical applications

Qifa Zhou^{a,*}, Kwok Ho Lam^b, Hairong Zheng^{c,*}, Weibao Qiu^c, and K. Kirk Shung^a

^aNIH Resource Center for Medical Ultrasonic Transducer Technology, and Department of Biomedical Engineering, University of Southern California, Los Angeles, CA 90089, United States

^bDepartment of Electrical Engineering, The Hong Kong Polytechnic University, Hunghom, Hong Kong

^cPaul C. Lauterbur Research Center for Biomedical Imaging, Shenzhen Institutes of Advanced Technology, Chinese Academy of Sciences, 1068 Xueyuan Ave., Nanshan, Shenzhen 518055, China

Abstract

Piezoelectric single crystals, which have excellent piezoelectric properties, have extensively been employed for various sensors and actuators applications. In this paper, the state-of-art in piezoelectric single crystals for ultrasonic transducer applications is reviewed. Firstly, the basic principles and design considerations of piezoelectric ultrasonic transducers will be addressed. Then, the popular piezoelectric single crystals used for ultrasonic transducer applications, including LiNbO₃ (LN), PMN-PT and PIN-PMN-PT, will be introduced. After describing the preparation and performance of the single crystals, the recent development of both the single-element and array transducers fabricated using the single crystals will be presented. Finally, various biomedical applications including eye imaging, intravascular imaging, blood flow measurement, photoacoustic imaging, and microbeam applications of the single crystal transducers will be discussed.

1. Introduction

1.1 Basic principles of the ultrasonic transducer

Ultrasonic transducers operate based on both converse and direct effects of piezoelectric materials in which the vibration would be produced upon the application of a potential difference across the electrodes and then the signal would be generated when receiving an echo. Consequently, piezoelectric elements play a very important role in transducer technology. For specific applications, proper piezoelectric materials are chosen according to a number of factors such as their piezoelectric performance, dielectric properties, elastic

© 2014 Elsevier Ltd. All rights reserved.

*Corresponding author. qifazhou@usc.edu (Q. Zhou), Hr.zheng@siat.ac.cn (H. Zheng).

Publisher's Disclaimer: This is a PDF file of an unedited manuscript that has been accepted for publication. As a service to our customers we are providing this early version of the manuscript. The manuscript will undergo copyediting, typesetting, and review of the resulting proof before it is published in its final citable form. Please note that during the production process errors may be discovered which could affect the content, and all legal disclaimers that apply to the journal pertain.

properties and stability. The selection criteria of these mechanical layers are presented in next section.

A transducer rings at its natural frequency once it is excited by an electrical source. Since the piezoelectric material itself exhibits much higher acoustic impedance (~30 MRayl) than that of biological tissue or water (~1.5 MRayl), a substantial part of the acoustic energy would be lost at the rear interface and not directed into the forward direction, resulting in poor resolution and sensitivity, if not properly matched acoustically. The transducer is usually treated as a three-port network including two mechanical ports and one electrical port as shown in Fig. 1.

The mechanical ports represent the front and back surfaces of the piezoelectric element and the electrical port represents the electrical connection of the piezoelectric element to the electrical source [1]. The front layer is known as an acoustic matching layer, which can improve the transducer performance significantly. Theoretical 100 % transmission is shown to occur for a sinusoidal acoustic wave when the matching layer thickness approaches $\lambda_m/4$ and acoustic impedance of the matching layer material Z_m is

$$Z_m = (Z_p Z_l)^{1/2} \quad (1)$$

where λ_m is the wavelength in the matching layer material, Z_p and Z_l are the acoustic impedances of piezoelectric material and the loading medium, respectively [2]. For wideband signal, the acoustic impedance of the single matching layer should be modified to be [3]

$$Z_m = (Z_p Z_l^2)^{1/3} \quad (2)$$

Sometimes, two matching layers may be used to further improve the front acoustic matching of the transducer. The acoustic impedances of the two layers should be [3]

$$Z_{m1} = (Z_p^4 Z_l^3)^{1/3} \quad (3)$$

$$Z_{m2} = (Z_p Z_l^6)^{1/7} \quad (4)$$

Mixing micro or nano scale powder into a polymer is one of the common approaches to fabricate matching layers. The acoustic impedance of the matching layer can be adjusted by the content of the powder [4, 5]. The scattering effect can be minimized efficiently by choosing proper size of the powder especially for high-frequency transducers. Coating a polymer onto the piezoelectric layer is also an alternative method to fabricate the matching layer. Parylene is a common polymer which minimizes the acoustic impedance mismatch and acts as a protecting layer as well [6].

In fact, 100 % transmission is impossible for only considering the front matching layer. Due to the acoustic mismatch between the air and the piezoelectric material, the reflected wave

reverberates inside the transducer element. This would cause long ring–down of the ultrasonic pulse, which is the so–called ringing effect. For imaging applications, it is highly undesirable to have a pulse with long duration. Backing layer can be used to damp out the ringing by absorbing part of the energy from the vibration of the back face. Besides minimizing the acoustic impedance mismatch, the backing layer can also act as a supporting layer of the fragile transducer element because of its relative rigid nature of the piezoelectric layer.

E–solder 3022 (Von Roll Isola Inc., New Haven, CT) is usually used as a backing layer material because of its electrical conductive nature, making it possible to be one of the electrodes of the transducer element. Besides, with its high attenuation (120 dB/mm at 30 MHz) and relatively low acoustic impedance (5.92 MRayl), low insertion loss can be achieved for the transducer with an optimal front matching layer (see table 1). Since there is a compromise between sensitivity and bandwidth, sometimes for specific applications, the acoustic impedance of the backing layer may be varied. Metal–loaded epoxy is another choice. By varying the content of metal powder (e.g. tungsten), the acoustic impedance of the composite can range from 8 to 20 MRayl [7].

The function of the electrical part is to maximize the energy transmission by matching the electrical characteristics of the transducer to the electrical source and the receiving circuits. Since the imaginary part of impedance would cause severe energy loss and reduction in bandwidth, the transducer input impedance should be real and the input resistance should match that of the source and receiver for the maximal power transmission [3, 10]. In a simple way, a series or parallel inductor is used to tune out the reactive part of the impedance at the center frequency of the transducer. However, the drawback may be the deformation of the pulse shape and reduction of bandwidth. A complicated electrical matching network may be implemented at the price of more energy loss.

The behavior of the ultrasonic transducer can be modeled using the existing one–dimensional circuit models. Among the models, the KLM model [11] is one of the popular one–dimensional models. With the KLM model, the transducer performance optimization may be understood in a more physically intuitive manner. PiezoCAD is commercial transducer simulation software based on the KLM model, which has extensively been used in transducer design. PZFlex, a finite element analysis software, is commercially available for simulation of arrays where inter–element cross–talk must be considered.

1.2 Critical material parameters for transducer design

Since the piezoelectric materials are anisotropic with permanent polarization, their parameters are expressed in matrix notation. The x , y , z directions are indicated by numbers 1, 2, 3. Each parameter generally has two subscripts that indicate the direction of the two related quantities, such as electric field and mechanical response for piezoelectricity, stress and strain for elasticity. Taking a piezoelectric strain constant d_{33} as an example, the first subscript represents an induced polarization in the 3 direction while the second one represents the mechanical response in the 3 direction. In the discipline of materials science, plenty of the parameters have to be used for describing various properties of the piezoelectric materials. Among them, three of the material properties are the most critical in

ultrasonic transducer design, which are dielectric, piezoelectric and acoustic properties. The related parameters are shown as below:

$$C_{33}^s = \frac{\varepsilon_{33}^s \varepsilon_0 A}{t} \quad (5)$$

$$k_t^2 = \frac{\text{Stored mechanical energy}}{\text{Input electrical energy}} = \frac{e_{33}^D{}^2}{c_{33}^D \varepsilon_{33}^s} \quad (6)$$

$$\omega_0 = \frac{2\pi c_p}{t} \quad (7)$$

$$Z_a = \rho c_p \quad (8)$$

where C^s , is the clamped capacitance; ε^s , the clamped dielectric permittivity; ε_0 , the dielectric permittivity of free space; A , the area; t , thickness; k_t , the thickness mode electromechanical coupling coefficient; e_{33}^D , the piezoelectric stress constant; c_{33}^D , the elastic constant; ω_0 , resonant frequency; c_p , the speed of sound inside the piezoelectric material; Z_a , acoustic impedance; ρ , the density.

As the piezoelectric material itself can be considered as a capacitor, the corresponding ultrasonic transducer is a capacitor structure. According to Eq. (5), the clamped capacitance of an ultrasonic transducer is determined by the clamped dielectric permittivity, the area and thickness of the piezoelectric material. To maximize the power transmission, the input electrical impedance of the ultrasonic transducer at the designated frequency should be real and its input resistance should match the electrical impedance of the source (normally 50 Ω in termination).

The electromechanical coupling coefficient k is an indicator of the effectiveness with which a piezoelectric material converts electrical energy into mechanical energy and vice versa. It is not a constant material parameter, but instead of depending upon the shape of the material. For example, the k coefficient of a material in a rod form is higher than that in a plate form [12]. In transducer design, a high k value is desirable for better energy conversion and improved bandwidth.

As shown in Eqs. (7) and (8), the resonant frequency and the acoustic impedance of a material are determined by the speed of sound inside itself which is an inherent property of the material. It is mentioned above that the impedance matching between the transducer and the propagating medium is very important to improve the transducer performance.

Besides selecting the appropriate piezoelectric material for a designated transducer, the configuration of the transducer element can also be tailored to approach the desired transducer performance. Piezoelectric 1–3 [13, 14] and 2–2 [15] composites are also commonly used in transducer technology. The higher k coefficients and better impedance matching can lead to higher transducer sensitivity and improved bandwidth.

1.3 The scope of the review

In this review, we focus on the design and fabrication of piezoelectric high– frequency single crystal ultrasonic transducers in various biomedical applications. Recent progress in the development and applications of piezoelectric single crystal ultrasonic transducers is presented. Section 2 reviews the single crystals commonly used for ultrasonic transducers. Section 3 presents different types of the transducers fabricated using the piezoelectric single crystals. Section 4 addresses the recent biomedical applications of piezoelectric single crystal ultrasonic transducers.

2. Single crystal materials for ultrasonic transducers

Due to their relatively high coupling capability and low dielectric loss, piezoelectric ceramics have been widely used in electromechanical applications [16]. Among the ceramics, $\text{Pb}(\text{Zr}, \text{Ti})\text{O}_3$ (PZT) ceramics with compositions near the morphotropic phase boundary (MPB) between the tetragonal and rhombohedral phases have the most outstanding performance [17], which become the popular choices for various high performance transducer applications. The polarizability is thought to be enhanced due to the coupling between two equivalent energy phases of the materials with the compositions near the MPB.

Another well–known piezoelectric family is lead–based relaxor family that was discovered in the 1950s [18]. The relaxor materials are complex perovskites with a chemical form of $\text{Pb}(\text{B}'\text{B}'')\text{O}_3$ ($\text{B}' = \text{Mg}^{2+}, \text{Zn}^{2+}, \text{Ni}^{2+}, \dots$, $\text{B}'' = \text{Nb}^{5+}, \text{Ta}^{5+}, \text{W}^{6+}, \dots$). Following the discovery of PZT, numerous $\text{Pb}(\text{B}'\text{B}'')\text{O}_3$ – PbTiO_3 materials were investigated [19, 20]. Similar to PZT, $\text{Pb}(\text{B}'\text{B}'')\text{O}_3$ – PbTiO_3 materials also have their MPB regions, resulting in relatively high dielectric permittivity, large piezoelectric strain and electromechanical coupling coefficients [21].

Besides the ceramics, piezoelectric single crystals have also been studied and developed. Unlike piezoelectric ceramics, single crystals have crystallographic axes. A plate cut with its surface perpendicular to the x –axis of a crystal is called x –cut, and so forth. The quality of the single crystals would depend on the purity of the starting materials, growth conditions and the orientation (cut direction) of the crystals.

Quartz and lithium niobate (LiNbO_3 , LN) are the traditional single crystals, however, they exhibit inferior piezoelectric performance compared to the PZT ceramics. Based on the development of relaxor–based system in ceramic engineering, the growth of corresponding single crystals was studied. Different from the PZT systems, most $\text{Pb}(\text{B}'\text{B}'')\text{O}_3$ – PbTiO_3 crystals were found to readily be grown by high temperature flux technique [22, 23]. With the excellent piezoelectric and electromechanical coupling performance, the relaxor–based single crystals have extensively been used in sensor [24, 25], actuator [26–28], and transducer [29–32] applications. As the performance of the single crystals depends significantly on the cut direction, the optimum conditions for specific applications can be tailor adjusted by the cut direction. Besides, the issues of grain size and porosity can be ignored for single crystals. The merit is significant especially for high–frequency transducer applications.

In this section, three single crystal materials including LN, $\text{Pb}(\text{Mg}_{1/3}\text{Nb}_{2/3})\text{-PbTiO}_3$ (PMN-PT), and $\text{Pb}(\text{In}_{1/2}\text{Nb}_{1/2})\text{-Pb}(\text{Mg}_{1/3}\text{Nb}_{2/3})\text{-PbTiO}_3$ (PIN-PMN-PT) single crystals are introduced, which are commonly used for medical ultrasound transducer applications. Their growth methods and critical parameters, such as the dielectric and piezoelectric properties, for transducer applications are described as follow.

2.1 LN single crystals

LN single crystal is a well-known piezoelectric single-crystal oxide material. Because of its stable and strong electro-mechanical and electro-optical coupling capabilities, LN single crystal has been extensively used in acoustic and electro-optical applications [33–35]. This material melts congruently with the composition reported to be between 48.35 to 48.60 mol % Li_2O [36, 37]. Almost all LN single crystal produced commercially is grown with congruent compositions using the Czochralski technique [38, 39]. Since the single crystal with desired off-congruent compositions is hard to produce by the Czochralski method due to segregation effects, vapor transport equilibrium (VTE) has also been studied to prepare the LN single crystal with controlled off-congruent compositions [40].

Compared to the lead-based PZT materials, a 36° rotated Y-cut LN single crystal exhibits a comparable electromechanical coupling coefficient ($k_t \sim 0.39$), a much lower dielectric permittivity ($\epsilon_{33}^s \epsilon_0 \sim 39$) and a higher longitudinal sound speed ($c_p \sim 7340$ m/s) and higher Curie temperature [8]. These characteristics make the LN single crystal an ideal and promising active element of sensitive large aperture single element transducers. Besides the traditional single-element transducer design, inversion layer transducers have also been studied using the LN single crystal [41]. Transducers in a wide range of frequency (10–100 MHz) have been studied using this kind of single crystal. With different design configurations, the transducers exhibit –6 dB bandwidth ranging from 57 to 80 % and insertion loss value ranging from 10 to 28 dB.

2.2 PMN-PT single crystals

PMN-PT is one of the important systems in a piezoelectric relaxor-based family. With the composition near the rhombohedral-tetragonal morphotropic phase boundary (MPB) shown in Fig. 2 [42–45], PMN-PT single crystal has extremely good dielectric and piezoelectric properties as a result of enhanced polarizability arising from the coupling between two equivalent energy states [46]. Numerous studies have been carried out to grow the PMN-PT single crystals. Most PMN-PT crystals can be grown based on the high temperature flux technique [46, 47] or Bridgeman method [48, 49].

With the ultrahigh piezoelectric performance ($d_{33} \sim 1500\text{--}2800$ pC/N) and electromechanical coupling capability ($k_{33} > 0.90$) [46, 50], the PMN-PT single crystals have been widely used in ultrasonic transducer technology [51–54]. As the dielectric permittivity of the PMN-PT single crystals is high ($\epsilon_{33}^s \epsilon_0 \sim 800$), it is highly desired for designing miniature (small aperture) transducers especially for intravascular imaging applications [55, 56]. The transducer applications will be further discussed in Section 4.

2.3 PIN–PMN–PT single crystals

Although the PMN–PT single crystal has outstanding piezoelectric performance, its relative low Curie temperature ($T_c \sim 130$ °C) limits high–temperature applications [57, 58]. Besides, as the rhombohedral–tetragonal phase transition (T_{rt}) appears in a temperature range of 60–95 °C, the electrical properties of the binary single crystal may also start to degrade [59, 60]. Consequently, a ternary single crystal PIN–PMN–PT with a high T_c of 200 °C was grown from the melt directly by the Bridgman method [61, 62]. The depoling temperature of the ternary single crystal was claimed to increase up to a range of 100–117 °C [63, 64]. Similar to the PMN–PT single crystals, the PIN–PMN–PT single crystals also have their MPB composition [65].

Since the PIN–PMN–PT single crystals near MPB composition have comparable piezoelectric performance ($d_{33} \sim 1500$ – 2700 pC/N; $k_{33} > 0.90$) to that of the PMN–PT single crystals [65], there is a recent trend towards the use of this kind of ternary single crystal for ultrasound transducer applications [66–69].

Table 2 summarizes the material properties of the common single crystals used in medical ultrasonic transducers. It is shown that the electromechanical performance and dielectric constant of the LN single crystal are much lower than those of the PMN–PT and PIN–PMN–PT single crystals. Nevertheless, with its low dielectric characteristics, the LN single crystal can be used to develop relatively large aperture transducers to match the electrical impedance (50Ω) for medical imaging application. Besides, the PIN–PMN–PT single crystal is shown to have comparable properties to the PMN–PT single crystal, but with much higher phase transition temperatures.

3. Single crystal ultrasonic transducers

Based on the applications, ultrasonic transducers are designed in a variety of forms and sizes. They range from single element pistons for mechanical scanning, linear arrays to multi–dimensional arrays for electronic scanning.

In this section, the single element and array transducers fabricated using the single crystals are introduced. The configurations, modeling and experimental performance of the transducers are presented.

3.1 Single–element transducers

Single–element piston transducers are the simplest ultrasonic transducer, which only involve one active element. In general, the single–element transducers can be classified as plane and focused for specific applications. Since the nature of the plane configuration limits the lateral resolution and sound intensity, focusing is utilized to improve the lateral resolution and performance in high–resolution imaging applications. Shaping the piezoelectric element or using a lens is a usual way to fabricate the focused transducers. Fig. 3 shows the schematic diagram of the lens–focused and press–focused transducers. As the LN single crystal exhibits stable performance, a study was conducted to study the configuration effect on the LN single crystal transducer [8]. It was found that the lens–focused transducers were reported to exhibit lower sensitivity due to attenuative losses and mechanical quality of the

lens. Nevertheless, because of the destructive pressing effect on the transducer element, the coupling and bandwidth performance was found to degrade for the press–focused transducers [8, 34].

Recently, an alternative method has been proposed to develop focused transducers. With a mechanical technique [54, 73], a front surface of an acoustic stack of single crystal with a backing layer can be dimpled to give a curvature for focusing. As shown in Fig. 4, even the material is a brittle single crystal, the dimpled surface is still smooth without the existence of any crack. Compared with the plane transducer, the transducer with a dimpled PMN–PT single crystal exhibits much larger electromechanical coupling coefficient, resulting in broader bandwidth and higher sensitivity.

Although focused transducers would give images with higher resolution, for some applications requiring miniature transducer, such as intravascular imaging [55, 74], plane transducer elements are commonly employed as shown in Fig. 5. It is not necessary to focus IVUS transducer because of seeing far acoustic field of vessel. Due to the limited size, the performance of the transducer including imaging resolution and sensitivity will have to be compromised.

With superior electromechanical coupling capability, PMN–PT and PIN–PMN–PT single crystals have extensively been utilized to fabricate single–element transducers. The details of the applications will be discussed in Section 4. A typical echo response of a 0.4–mm aperture PMN–PT needle transducer is given in Fig. 6 [75]. Because of the excellent intrinsic nature of the PMN–PT single crystal, the transducer was found to exhibit a high effective electromechanical coupling coefficient k_{eff} of 0.58. A –6 dB bandwidth of 45 % and an insertion loss of 15 dB were obtained with double matching layers (2–3 μm silver particles/Insulcast 501 and Insulcure 9, and parylene).

Fig.7 shows the measured pulse–echo characteristics of PIN–PMN–PT single element transducers with different center frequencies [67]. Both transducers were found to exhibit strong echo response with a –6 dB bandwidth of ~47 %. Insertion loss of the 35 MHz and 60 MHz transducers was calculated to be 15 dB and 17 dB, respectively.

The results show that both the PMN–PT and PIN–PMN–PT single crystals are promising materials for ultrasonic transducer applications. Besides the single–phase active element, biphasic composites have also been extensively studied in various sensor and actuator applications [76–79] because of the outstanding performance combined with monolithic piezoelectric single crystals (or ceramics) and passive polymers. Among various types of composites, a piezoelectric 1–3 composite, consists of piezoelectric rods embedded in a passive epoxy matrix, has widely been studied for biomedical imaging applications [80–82]. Traditionally, dice–and–fill method was employed to develop low– frequency (<10 MHz) transducers. However, due to the physical limitation of blade and brittleness of the active materials, the traditional method cannot be used to develop high– frequency (>30 MHz) transducers. With the increasing demand of high–frequency ultrasonic applications, a novel etch–and–fill technique has been developed recently [82]. With using the ICP (Inductively

Coupled Plasma)–RIE (Reactive Ion Etching) dry etching technique, PMN–PT single crystal can be etched to a periodic rod pattern with a sidewall angle of $>85^\circ$ as shown in Fig. 8.

The high–frequency (35 MHz) 1–3 composite with 45 % single crystal volume fraction was fabricated after filled the kerfs with Epotek–301 epoxy. From the measured impedance/phase spectrum as shown in Fig.9, k_t of the composite transducer was calculated to be 0.81 which is substantially higher than that of the bulk PMN–PT transducer [82]. The measured pulse–echo characteristics (shown in Fig.10) of the composite transducer show that the composite transducer exhibited a center frequency of 32 MHz with outstanding performance such as –6 dB bandwidth of 110 % and insertion loss of 18 dB [82].

3.2 Array transducers

Arrays are transducer assemblies with more than one element. These elements may be rectangular in shape and arranged in a line (called linear or one–dimensional array); square in shape and arranged in rows and columns (called two–dimensional array); or ring shaped and arranged concentrically (called annular array).

Compared to the single–element transducers, array transducers are desired in clinical applications because of the clinical convenience, increased frame rates, and the capability to focus the beam dynamically [83]. The array performance can be enhanced by a number of schemes including electrical tuning, acoustic stack design configuration and proper material selection.

3.2.1 Linear array transducers—The schematic diagram of a linear array transducer is shown in Fig. 11. Generally, the array is fabricated by mechanically dicing a bulk piezoelectric material. To eliminate the cross–talk between neighboring array elements, a highly acoustically attenuating material is used to fill the kerf.

Both the PMN–PT and PIN–PMN–PT single crystals have been studied for array transducer applications. A 32–element linear array transducer was fabricated for performance comparison of these two single crystals [85]. Aluminum oxide loaded epoxy and polyurethane were used as the first and second matching layer, respectively. An acoustic lens was attached on the front face of the array to give a focal length of about 6 cm. It was found that the PIN–PMN–PT single crystal array transducer had a performance comparable to the PMN–PT one. However, the PMN–PT array transducer degraded beyond a phase transition temperature from rhombohedral to tetragonal ($>100^\circ\text{C}$) and then malfunctioned beyond its Curie temperature ($<160^\circ\text{C}$) as shown in Fig. 12. As the PIN–PMN–PT single crystal has relatively higher transition temperatures, the array fabricated from this material presumably should be capable of enduring higher temperatures.

Besides the materials study, the acoustic design configuration has also been studied by using the PMN–PT single crystal as the transducer element of a 4–MHz phased array [84]. Fig. 13 shows that the transducer was found to exhibit a strong thickness–mode resonance.

The electromechanical coupling factor k_{33} of the transducer approached 0.80. With using double matching layers (2–5 μm alumina particles/Epotek 301, and Epotek 301) and heavy

backing layer ($5\ \mu\text{m}$ tungsten particles/microbubbles/Epotek 301), the PMN–PT single crystal phased array was found to exhibit a $-6\ \text{dB}$ bandwidth of 110 % as shown in Fig. 14.

3.2.2 Radial array transducers—Compared to the images acquired by a traditional transducer being placed directly on the skin overlaying the target organ(s), it would be much accurate and detailed while the imaging is performed inside the body. Endoscopic ultrasound is a technique which combines endoscopy and ultrasound to obtain images and information of the organs inside the body such as lung and pancreas [86, 87]. In most EUS systems, a single–element transducer is employed to be mechanical driven by a motor so as to rotate inside the endoscope to form an image by 360° scanning. Although the fabrication method of the single–element transducer is relatively easy, the imaging frame rate would be limited by the mechanical scanning system. The other alternative way is to develop a radial array transducer which provides an image by electronic scanning. It can solve the limitation of the frame rate, but raises the challenges in fabrication process.

For the radial array transducers, tiny array elements distribute uniformly on the curved surface as shown in Fig. 15. If the transducer is fabricated using the wrapping method, the elements should be subject to a bending force so that the fragile piezoceramics are likely to be broken during the fabrication process. Excluding the fragile ceramics and low dielectric piezopolymers, polymer–based composites seem to be a good choice for being an active material of the radial array transducers.

The PMN–PT single crystal 1–3 composite fabricated using the dice–and–fill method [88] has been developed for endoscopic transducer applications [89]. To ease the wrapping process, both the matching ($5\ \mu\text{m}$ alumina particles/EPO–TEK 301) and backing ($2\ \mu\text{m}$ tungsten particles/microbubbles/LEK–0350) layers were designed to be highly flexible. As shown in Fig. 16, the three–layer laminate with 64 array elements was wrapped on a copper cylinder to form the radial array transducer. The copper cylinder was electrically connected to the bottom electrodes of the array elements and the ground wires of the coaxial cables by using electrically conductive epoxy. After that, a $1\ \mu\text{m}$ –thick parylene C (supplied by Specialist Coating Systems, Indianapolis, IN) was deposited onto the arrays as a waterproof coating. A photograph of the radial array transducer prototype is shown in Fig. 17.

Fig. 18 shows the electrical impedance magnitude and phase angle for the PMN–PT 1–3 composite radial array element. The resonance mode was strong and its corresponding effective electromechanical coupling coefficient was calculated to be 0.69. The time domain receive–echo response and frequency spectrum of the single array element are shown in Fig. 19. By picking ten array elements for measurement, the average center frequency of the transducer was found to be 6.91 MHz. The average $-6\ \text{dB}$ bandwidth was calculated to be 102 %, which was much higher than that of the common commercial PZT array transducers (70 %).

4. Biomedical applications

4.1 High resolution eye imaging

High frequency ultrasound, which offers better resolution, has had a significant impact upon clinical imaging of the eye diseases. Single crystal-based transducer is usually chosen to achieve improved imaging performance. High frequency ultrasound allows the anterior segment of the eye to be visualized. Fig. 20 shows the ultrasound images of the human eye acquired with a 75-MHz LN transducer, which yields superior resolution over traditional transducers [90]. As shown in Fig. 20(a), the flap is seen mainly as a discontinuity in stromal backscatter between the stromal component of the flap and residual stroma. Discontinuities are seen in Bowman's layer, indicative of microfolds or breaks. Fig. 20(b) shows the image of the nasal quadrant of the anterior segment, encompassing the peripheral cornea, iris, conjunctiva and sclera as well as part of the lens. The results demonstrate that high frequency ultrasound could provide sufficient sensitivity to visualize the detailed structure of the eye. 75 MHz MBF images of quadrant of LASIK-treated eye. Iris (I), ciliary processes (CP), conjunctiva (C), sclera (S), lens surface (L) and flap insertion point (F) are indicated [90].

4.2 Intravascular imaging

Atherosclerosis is a principal consequence of cardiovascular diseases resulting in the narrowing of the arteries, which can lead to ischemia of the heart. Clinically, plaque is considered as the main determinants of luminal narrowing in atherosclerosis. Intravascular ultrasound (IVUS) imaging, which can assess the morphological properties of blood vessels directly by inserting a miniature catheter into the arteries, has been increasingly used for clinical investigations. Due to the anatomical restriction, the ultrasound transducer on the tip of the catheter must have to have a very small size, which makes it very challenge to design a high performance ultrasonic transducer. With their many advantages, single crystals are highly desired for developing miniature transducers of superior performance. Fig. 21(a) shows an intravascular image acquired by a 32-MHz PMN-PT single crystal catheter [91]. The measured -6 dB bandwidth and the insertion loss are 62.7 % and 25 dB, respectively. Different layers of the artery can be clearly identified in the ultrasound image. Fig. 21(b-c) presents the intravascular images from porcine vessel taken by an IVUS transducer fabricated using a 1-3 composite PMN-30PT single crystal [55]. The vessel wall itself consists of a medial layer of about 2-3 mm thickness and is lined on the inside with the intima layer of about 100 μm . The images show a significantly fine blood speckle and allow for visual differentiation of vessel structures such as the intima (Fig. 21(b)) and stent struts (Fig. 21(c)).

4.3 Skin imaging

High resolution and noninvasive imaging of skin morphology and pathology is very important in dermatology. High frequency ultrasound has become an invaluable diagnostic tool for measuring the size of tumors and inflammatory processes. For preoperative planning, the safety distance can easily be determined with the information acquired by high frequency ultrasound [92]. In addition, skin echogenicity, burn scars, wound healing, skin aging, and skin tumors can also be studied with high resolution ultrasound [93]. Single

crystal based transducer can also be used for skin assessment. Fig. 22 shows an *in vivo* skin image acquired by a 50-MHz LN transducer with a focal length of 9.3 mm, an aperture size of 4.5 mm, and a relative -6 dB bandwidth of 47 %. Different layers including epidermis, dermis, and hypodermis are visualized clearly by single crystal based ultrasonic transducer [94].

4.4 Blood flow measurement

Due to high sensitivity of single crystal transducers, the blood flow pattern could be acquired with a high accuracy. Fig. 23 shows the images of low speed blood flow from an (a) animal and (b) human *in vivo* acquired with a PMN-PT single crystal based high frequency (45 MHz) ultrasonic needle transducer. Fig. 23(a) presents two flow patterns from vein and artery of retina in a rabbit eye simultaneously. Blood flow in both the retinal vein and retinal artery with a diameter less than 200 μm was measured in real time [95]. The Doppler spectrosonogram from the artery can be separated from the one in vein based on the flow directions and the flow patterns. The vein blood flow had lower and relatively constant velocity while the artery blood flow showed a higher and pulsatile velocity pattern. Fig. 23(b) shows an *in vivo* spectrogram acquired from a vein at the back of a human hand. The flow pattern can be visualized with a velocity around 10 mm/s [96]. Recently, a 40 MHz PMN-PT single crystal needle transducer was also used to monitor the blood flow velocity near the occlusion site in the rabbit ear vein so as to determine the effect of sonothrombolysis [97]. A Doppler spectrogram shown in Fig. 24 demonstrates that the customized high-frequency transducer can monitor the recanalization of occluded veins of a small animal.

Besides the PMN-PT single crystal, LN single crystal was also employed for developing lightweight single-element transducers for high frame rate imaging system [98]. Fig. 25 shows Doppler waveforms acquired from a four-week mouse heart. Guided by the B-mode imaging, the pulsed-wave Doppler waveforms display the blood flow in the left ventricle and aorta as shown in Figs. 25(a) and 25(b), respectively.

4.5 Photoacoustic imaging

Photoacoustic imaging makes use of the physical effect of the generation of acoustic waves by the absorption of optical energy. It has been proposed for a variety of applications in biomedical field. Since the acoustic wave is the signal acquired for imaging, an ultrasonic transducer is critical component in photoacoustic imaging. Given the superior properties of Single crystals, they have been recently used in the design of endoscopic and intravascular probes for multi-modality imaging that combines ultrasound and photoacoustics.

Fig. 26 shows the integrated probe that produces photoacoustic and ultrasound images for *in vivo* endoscopy [99]. LN single crystal based focused ultrasonic transducer (~36 MHz, 65% fractional bandwidth) with double layer acoustic matching scheme was employed to improve the overall image quality, transverse resolution and the signal sensitivity. Fig. 27 shows co-registered *in vivo* images obtained from a rat colon [99]. Three-dimensionally rendered ultrasonic-photoacoustic image was acquired. Photoacoustic imaging shows densely distributed blood vasculature in the colon wall, whereas ultrasonic imaging shows

the tissue anatomy in the mucosal and submucosal layers and other mesenteric tissues entangled around the tract (Fig. 27(a)). The right side of this image is closer to the anus, and the negative axis corresponds to the ventral direction of the animal. The red and green colors correspond to photoacoustic and ultrasonic signals, respectively. It provides high-resolution vasculature information in the gastrointestinal tract and clearly shows optical and mechanical contrast differences.

4.6 Manipulation of small particles

Besides conventional imaging applications, ultrasonic transducers have also been developed for microbeam application in recent years. Ultrahigh frequency (UHF) ultrasonic transducers that generate tightly focused microbeams can be developed as acoustic tweezers to manipulate micro-particles. Compared to the optical methods, these acoustic devices are simpler and of lower cost. The main advantages are that the acoustic microbeam is safer to the biological samples than the focused laser beam and it is capable of penetrating light opaque media.

For these applications, UHF (200-MHz) press-focused ultrasonic transducers were fabricated using LN single crystal [100]. With an f -number of 1.6, the transducer exhibited a lateral beam width of 16.8 μm , which was close to the theoretical value. Fig. 28 shows the capability of the 200-MHz microbeam devices in trapping a 5 μm single microsphere. It was shown that the single microsphere (in a red circle) was manipulated within a range of tens of micrometers along with the movement of the microbeam device. Besides the micro-particle manipulation, the ultrasound microbeam has also demonstrated the capability of other biomedical applications recently, such as measurement of red blood cell deformation [101] and breast cancer cells stimulation [102].

Single crystal also finds value in manipulation of micro-particles with surface acoustic wave (SAW) device. Fig. 29 shows a microfluidic device fabricated by 0.5 mm LN crystal. A pair of interdigital transducer electrodes (IDT) made of 200 nm aluminum was deposited on the LN material for surface acoustic wave generation and detection. The resonance frequency is 39.2 MHz for this design [103]. Fig. 30 demonstrates the manipulation of micro-bubble (MB) cluster with a LN-based device. The trapped MBs were moved in a square trajectory. Initially, the MBs were suspended in a solution uniformly and they were almost invisible [Fig. 30(a)] because the individual bubble was small and dim. When applying the ultrasonic wave, the MBs aggregated into clusters (within about 200 ms) [Fig. 30(b)] forming a two-dimensional grid structure. Fig. 30(c) shows the enlarged image of the MB clusters inside the rectangle (dash line) and the right cluster is the virtual image caused by the aberration of the microscope. The MB cluster moved along the positive Y-axis or X-axis direction by varying the relative phase of the two acoustic sources from opposite transducers after changing the wave [Fig. 30(d-f)]. Noted that almost all the MBs were concentrated at the pressure nodes and the trapped MB clusters can be transported in parallel. Therefore, it may be possible to manipulate a large number of bioparticles in concert in the ultrasonic field based on the same principle. In addition, the number of clusters inside of the microchannel can also be adjusted by changing the ultrasonic frequency [104].

5. Conclusions

This article reviews the recent developments of piezoelectric single crystals for the design and fabrication of ultrasonic transducers in various biomedical applications. Three different types of single crystals including LN, PMN–PT and PIN–PMN–PT have been discussed. Because of their superior performance, the single crystal–based ultrasonic transducers have been employed in a wide range of biomedical applications. Besides conventional imaging applications, these ultrasonic transducers have also been combined with optics to provide structural and functional imaging simultaneously. Moreover, recent advances on microbeam applications of the single crystal–based transducers have also been discussed. It is envisioned that the role of piezoelectric single crystals in biomedical and other applications will become increasingly important in the years to come.

Acknowledgments

This work has been supported by National Institute of Health (NIH) Grants Nos. P41–EB02182, R01CA157277–01 and R01EB010090. This work has also been partially supported by National Science Foundation of China (NSFC Grant Nos. 11325420 to H. Zheng).

References

1. Kino, GS. *Acoustic Waves*. Prentice Hall; Englewood Cliffs, NJ: 1987.
2. Kinsler, LE.; Frey, AR.; Coppens, AB.; Sanders, JV. *Fundamentals of Acoustics*. 3rd ed.. John Wiley & Sons; New York: 1982.
3. Desilets CS, Fraser JD, Kino GS. The design of efficient broad–band piezoelectric transducer. *IEEE Trans Sonics Ultrason*. 1978; 25:115–25.
4. Zhou QF, Cha JH, Huang Y, Zhang R, Cao W, Shung KK. Alumina/epoxy nanocomposite matching layers for high–frequency ultrasound transducer application. *IEEE Trans Ultrason Ferroelect Freq Contr*. 2009; 56(1):213–9.
5. Tiefensee F, Becker Willinger C. Nanocomposite materials for high frequency ultrasound matching layers. *Proc IEEE Ultrason Symp*. 2009:1719–21.
6. Wang H, Ritter TA, Cao W, Shung KK. *Passive Materials for High Frequency Ultrasonic Transducers*. Proceedings of the SPIE Medical Imaging, Ultrasonic Transducer Imaging. 1999; 3664:35–42.
7. Webster RA, Button TW, Meggs C, MacLennan, Cochran S. Passive materials for high frequency ultrasound components. *Proc IEEE Ultrason Symp*. 2007:1925–8.
8. Cannata JM, Ritter TA, Chen WH, Silverman RH, Shung KK. Design of efficient, broadband single–element (20–80 MHz) ultrasonic transducers for medical imaging applications. *IEEE Trans Ultrason Ferroelect Freq Contr*. 2003; 50(11):1548–57.
9. Wang HF, Ritter TA, Cao WW, Shung KK. High frequency properties of passive materials for ultrasonic transducers. *IEEE Trans Ultrason Ferroelect Freq Contr*. 2001; 48(1):78–84.
10. Goldberg, RL.; Smith, SW. *Transducers*. In: Bronzino, J., editor. *The biomedical engineering handbook*. CRC Press; Boca Raton (FL): 1994. p. 1077–92.
11. Krimholtz R, Leedom D, Matthei G. New equivalent circuits for elementary piezoelectric transducers. *Electron Lett*. 1970; 6:398–9.
12. Kim M, Kim J, Cao WW. Experimental technique for characterizing arbitrary aspect ratio piezoelectric resonators. *Appl Phys Lett*. 2006; 89:162910.
13. Smith WA, Auld BA. Modeling 1–3 composite piezoelectrics–thickness mode oscillations. *IEEE Trans Ultrason Ferroelect Freq Contr*. 1991; 38(1):40–7.
14. Chan HLW, Unsworth J. Simple model for piezoelectric ceramic/polymer 1–3 composites used in ultrasonic transducer applications. *IEEE Trans Ultrason Ferroelect Freq Contr*. 1989; 36(4):434–41.

15. Liu RB, Harasiewicz KA, Foster FS. Interdigital pair bonding for high frequency (20–50 MHz) ultrasonic composite transducers. *IEEE Trans Ultrason Ferroelect Freq Contr.* 2001; 48(1):299–306.
16. Haertling GH. Ferroelectric ceramics: history and technology. *J Am Ceram Soc.* 1999; 82(4):797–818.
17. Jaffe B, Roth RS, Marzullo S. Properties of piezoelectric ceramics in the solid– solution series lead titanate–lead zirconate–lead oxide: tin oxide and leadtitanate–lead hafnate. *J Res Natl Bur Standard.* 1955; 55:239–54.
18. Smolenskii GA, Agranovskaya AI. Dielectric polarization and losses of some complex compounds. *SovPhys Tech Phys.* 1958; 3:1380–2.
19. Berlincourt DA, Cmolik C, Jaffe H. Piezoelectric properties of polycrystalline lead titanate zirconate compositions. *Proc IRA.* 1960; 48:220–9.
20. Galasso F, Darby W. Preparation of single crystals of complex perovskite ferroelectric and semiconducting compounds. *InorgChem.* 1965; 4(1):71–3.
21. Cross LE. Relaxor ferroelectrics. *Ferroelectrics.* 1987; 76:241–67.
22. Mulvihill ML, Park SE, Risch G, Li Z, Uchino K, Shrout TR. The role of processing variables in the flux growth of lead zinc niobate–lead titanaterelaxor ferroelectric single crystals. *Jpn J ApplPhys1.* 1996; 35:3984–90.
23. Park SE, Mulvihill ML, Risch G, Shrout TR. The effect of growth conditions on the dielectric properties of $Pb(Zn_{1/3}Nb_{2/3})O_3$ single crystals. *Jpn J ApplPhys 1.* 1997; 36:1154–8.
24. Lam KH, Lo CY, Dai JY, Chan HLW, Luo HS. Enhanced ME effect in a stress– biased PMN–PT single crystal/Terfenol–D alloy magnetolectric sensor. *J ApplPhys.* 2011; 109(2):024505.
25. Zhao XY, Wu X, Liu LH, Luo HS, Neumann N, Yu P. Pyroelectric performances of relaxor–based ferroelectric single crystals and related infrared detectors. *Phys Status Solidi A–Appl Mat.* 2011; 208(5):1061–7.
26. Park SE, Shrout TR. Relaxor based ferroelectric single crystals for electro–mechanical actuators. *Mater Res Innovations.* 1997; 1(1):20–5.
27. Roberts DC, Li HQ, Steyn JL, Turner KT, Mlcak R, Saggere L, Spearing SM, Schmidt MA, Hagood NW. A high–frequency, high–stiffness piezoelectric actuator for microhydraulic applications. *Sensor Actuat A–Phys.* 2002; 97(8):620–31.
28. Lam KH, Chan HLW, Luo HS, Yin QR, Yin ZW. Piezoelectrically actuated ejector using PMN–PT single crystal. *Sensor Actuat A–Phys.* 2005; 121:197–202.
29. Park SE, Shrout TR. Characteristics of relaxor–based piezoelectric single crystals for ultrasonic transducers. *IEEE Trans Ultrason Ferroelect Freq Contr.* 1997; 44(5):1140–7.
30. Ritter T, Geng XC, Shung KK, Lopath PD, Park SE, Shrout TR. Single crystal PZN/PT–polymer composites for ultrasound transducer applications. *IEEE Trans Ultrason Ferroelect Freq Contr.* 2000; 47(4):792–800.
31. Ren KL, Liu YM, Geng XC, Hofmann HF, Zhang QMM. Single crystal PMN–PT/epoxy 1–3 composite for energy–harvesting application. *IEEE Trans Ultrason Ferroelect Freq Contr.* 2006; 53(3):631–8.
32. Amin A, McLaughlin E, Robinson H, Ewart L. Mechanical and thermal transitions in morphotropic PZN–PT and PMN–PT single crystals and their implication for sound projectors. *IEEE Trans Ultrason Ferroelect Freq Contr.* 2007; 54(6):1090–5.
33. Gnewuch H, Zayer NK, Pannell CN, Ross GW, Smith PGR. Broadband monolithic acousto–optic tunable filter. *Optics Letters.* 2000; 25(5):305–7. [PubMed: 18059862]
34. Snook KA, Zhao JZ, Alves CHF, Cannata JM, Chen WH, Meyer JJ, Ritter TA, Shung KK. Design, fabrication, and evaluation of high frequency, single–element transducers incorporating different materials. *IEEE Trans Ultrason Ferroelect Freq Contr.* 2002; 49(2):169–76.
35. Chen F. Photonic guiding structures in lithium niobate crystals produced by energetic ion beams. *J App Phys.* 2009; 106(8):081101.
36. O'Bryan HM, Gallagher PK, Brandle CD. Congruent composition and Li–rich phase boundary of $LiNbO_3$. *J Am Ceram Soc*1985. 68:493–6.

37. Baumann J, Rudolph P, Krabe D, Schalge R. Orthoscopic investigation of the axial optical and compositional homogeneity of Czochralski grown LiNbO₃ crystals. *J Cryst Growth*. 1993; 128:903–8.
38. Bordui PF, Norwood RG, Bird CD, Calvert GD. Compositional uniformity in growth and poling of large-diameter lithium niobate crystals. *J Cryst Growth*. 1991; 113:61–8.
39. Kitamura K, Yamamoto JK, Iyi N, Kimura S, Hayashi T. Stoichiometric LiNbO₃ single crystal growth by double crucible Czochralski method using automatic powder supply system. *J Cryst Growth*. 1992; 116:327–32.
40. Bordui PF, Norwood RG, Jundt DH, Fejer MM. Preparation and characterization of off-congruent lithium niobate crystals. *J Appl Phys*. 1992; 71:875–9.
41. Yachi M, Ono M. The third overtone resonator using 36° rotated Y cut LiNbO₃ crystal. *Proc IEEE Ultra Symp*. 1995:1003–6.
42. Yamada T, Niizeki N, Toyoda H. Piezoelectric and elastic properties of lithium niobate single crystals. *Jpn J Appl Phys*. 1967; 6(2):151–5.
43. Zhou QF, Cannata JM, Guo HK, Huang CZ, Marmarelis VZ, Shung KK. Half-thickness inversion layer high-frequency ultrasonic transducers using LiNbO₃ single crystal. *IEEE Trans Ultrason Ferroelect Freq Contr*. 2005; 52(1):127–33.
44. Park SE, Hackenberger W. High performance single crystal piezoelectrics: applications and issues. *Curr Opin Solid State Mat Sci*. 2002; 6:11–8.
45. Yamashita Y. Large electromechanical coupling factors in perovskite binary material system. *JpnJApplPhys*. 1994; 33:5328–31.
46. Zhang SJ, Li F. High performance ferroelectric relaxor-PT single crystals: status and perspective. *J Appl Phys*. 2012; 111:031301.
47. Zhang SJ, Shrout TR. Relaxor-PT single crystals: observations and developments. *IEEE Trans UltrasonFerroelectFreqContr*. 2010; 57:2138–46.
48. Zhang SJ, Li F, Luo J, Sahul R, Shrout TR. Relaxor-PbTiO₃ single crystals for various applications. *IEEE Trans UltrasonFerroelectFreqContr*. 2013; 60:1572–80.
49. Park SE, Shrout TR. Ultrahigh strain and piezoelectric behavior in relaxor based ferroelectric single crystals. *JApplPhys*. 1997; 82:1804–11.
50. Li F, Zhang S, Xu Z, Wei X, Luo J, Shrout TR. Composition and phase dependence of the intrinsic and extrinsic piezoelectric activity of domain engineered (1-x)Pb(Mg_{1/3}Nb_{2/3})O₃-xPbTiO₃ crystals. *J Appl Phys*. 2010; 108:034106. [PubMed: 20806001]
51. Lee HJ, Zhang S, Luo J, Li F, Shrout TR. Thickness dependent properties of relaxor-PbTiO₃ ferroelectrics for ultrasonic transducers. *Adv Funct Mater*. 2010; 20:3154–62. [PubMed: 21954374]
52. Li F, Zhang S, Xu Z, Wei X, Luo J, Shrout TR. Critical property in relaxor-PbTiO₃ single crystals --- shear piezoelectric response. *Adv Funct Mater*. 2011; 21:2118–28. [PubMed: 21960942]
53. Shrout TR, Chang ZP, Kim N, Markgraf S. Dielectric behavior of single crystals near the (1-x)Pb(Mg_{1/3}Nb_{2/3})O₃-(x)PbTiO₃ morphotropic phase boundary. *Ferroelect Lett*. 1990; 12(3):63–9.
54. Shimanuki S, Saitoh S, Yamashita Y. Single crystal of the Pb(Zn_{1/3}Nb_{2/3})O₃-PbTiO₃ system grown by the vertical Bridgeman method and its characterization. *Jpn J Appl Phys*. 1998; 37:3382–5.
55. Xu GS, Luo HS, Guo YP, Gao YQ, Xu HQ, Qi ZY, Zhong WH, Yin ZW. Growth and piezoelectric properties of Pb(Mn_{1/3}Nb_{2/3})O₃-PbTiO₃ crystals by the modified Bridgeman technique. *Solid State Commun*. 2001; 120(7–8):321–4.
56. Zhu S, Jiang B, Cao W. Characterization of piezoelectric materials using ultrasonic and resonant techniques. *Proc SPIE*. 1998; 3341:154.
57. Cheng KC, Chan HLW, Choy CL, Yin QR, Luo HS, Yin ZW. Single crystal PMN-0.33PT/epoxy 1–3 composites for ultrasonic transducer applications. *IEEE Trans Ultrason Ferroelect Freq Contr*. 2003; 50(9):1177–83.
58. Lau ST, Lam KH, Chan HLW, Choy CL, Luo HS, Yin QR, Yin ZW. Ferroelectric lead magnesium niobate-lead titanate single crystals for ultrasonic hydrophone applications. *Mat Sci Eng B*. 2003; 111(1):25–30.

59. Edwards G, Chan HLW, Batten A, Lam KH, Luo HS, Scott DA. PMN–PT single–crystal transducer for non–destructive evaluation. *Sensor Actuat A–Phys.* 2006; 132(2):434–40.
60. Lam KH, Chen Y, Cheung KF, Dai JY. PMN–PT single crystal focusing transducer fabricated using a mechanical dimpling technique. *Ultrasonics.* 2011; 52(1):20–4. [PubMed: 21705037]
61. Yuan J, Rhee S, Jiang XN. 60 MHz PMN–PT based 1–3 composite transducer for IVUS imaging. *Proc IEEE Ultra Symp.* 2008:682–5.
62. Yang HC, Yin JC, Hu CH, Zhou QF, Cannata J, Chen ZP, Shung KK. Novel biomedical imaging that combines intravascular ultrasound (IVUS) and optical coherence tomography (OCT). *Proc IEEE Ultra Symp.* 2008:1769–72.
63. Luo H, Xu G, Wang P, Yin Z. Growth and characterization of relaxor ferroelectric PMNT single crystal. *Ferroelectrics.* 1999; 231:97–102.
64. Harada K, Hosono Y, Saitoh S, Yamashita Y. Crystal growth of $\text{Pb}(\text{Zn}_{1/3}\text{Nb}_{2/3})_{0.91}\text{Ti}_{0.09}\text{O}_3$ using a crucible by the supported Bridgeman method. *Jpn J Appl Phys1.* 2000; 39:3117–20.
65. Hosono Y, Harada K, Kobayashi T, Itsumi K, Izumi M, Yamashita Y, Ichinose N. Temperature dependence of dielectric and piezoelectric properties of $\text{Pb}(\text{Zn}_{1/3}\text{Nb}_{2/3})\text{O}_3$ – PbTiO_3 piezoelectric single crystals. *JpnJApplPhys1.* 2002; 41:3808–11.
66. Zhang S, Luo J, Hackenberger W, Shrout TR. Characterization of $\text{Pb}(\text{Zn}_{1/3}\text{Nb}_{2/3})\text{O}_3$ – PbTiO_3 ferroelectric crystal with enhanced phase transition temperatures. *J Appl Phys.* 2008; 104:064106.
67. Guo Y, Luo H, He T, Yin Z. Peculiar properties of a high Curie temperature $\text{Pb}(\text{In}_{1/2}\text{Nb}_{1/2})\text{O}_3$ – PbTiO_3 single crystal grown by the modified Bridgeman technique. *Solid State Commun.* 2002; 123(9):417–20.
68. Xu G, Chen K, Yang D, Li J. Growth and electrical properties of large size $\text{Pb}(\text{In}_{1/2}\text{Nb}_{1/2})\text{O}_3$ – $\text{Pb}(\text{Mn}_{1/3}\text{Nb}_{2/3})\text{O}_3$ – PbTiO_3 crystals prepared by the vertical Bridgeman technique. *Appl Phys Lett.* 2007; 90:032901.
69. Zhang S, Li F, Sherlock NP, Luo J, Lee HJ, Xia R, Meyer RJ, Hackenberger W, Shrout TR. Recent development on high Curie temperature PIN–PMN–PT ferroelectric crystals. *J Cryst Growth.* 2011; 318:846–850.
70. Tian J, Han P, Huang X, Pan H. Improved stability of piezoelectric crystals grown in the lead indium niobate–lead magnesium niobate–lead titanate system. *Appl Phys Lett.* 2007; 91:222903.
71. Chen Y, Lam KH, Zhou D, Gao XS, Dai JY, Luo HS, Chan HLW. Temperature and electric field dependence of the dielectric property and domain evolution in $[001]$ –oriented $0.34\text{Pb}(\text{In}_{1/2}\text{Nb}_{1/2})\text{O}_3$ – $0.25\text{Pb}(\text{Mg}_{1/3}\text{Nb}_{2/3})\text{O}_3$ – 0.41PbTiO_3 single crystal. *J Appl Phys.* 2011; 109:014111.
72. Liu X, Zhang S, Luo J, Shrout TR, Cao W. Complete set of material constants of $\text{Pb}(\text{In}_{1/2}\text{Nb}_{1/2})\text{O}_3$ – $\text{Pb}(\text{Mg}_{1/3}\text{Nb}_{2/3})\text{O}_3$ – PbTiO_3 single crystal with morphotropic phase boundary composition. *J Appl Phys.* 2009; 106:074112.
73. Zhou QF, Zhu BP, Wu DW, Hu CH, Cannata JM, Tian J, Han PD, Shung KK. PIN–PMN–PT single crystal high frequency ultrasound transducers for medical applications. *Proc IEEE Ultra Symp.* 2008:1433–6.
74. Sun P, Zhou QF, Zhu BP, Wu DW, Hu CL, Cannata JM, Tian J, Han PD, Wang GF, Shung KK. Design and fabrication of PIN–PMN–PT single–crystal high–frequency ultrasound transducers. *IEEE Trans Ultrason Ferroelect Freq Contr.* 2009; 56(12):2760–3.
75. Lee HJ, Zhang SJ, Shrout TR. Scaling effects of relaxor– PbTiO_3 crystals and composites for high frequency ultrasound. *J Appl Phys.* 2010; 107:124107. [PubMed: 20644658]
76. Chen Y, Lam KH, Zhou D, Cheng WF, Dai JY, Luo HS, Chan HLW. High–frequency PIN–PMN–PT single crystal ultrasonic transducer for imaging applications. *Appl Phys A–Mater.* 2012; 108:987–91.
77. Zhang R, Jiang B, Cao W. Elastic, piezoelectric, and dielectric properties of multidomain $0.67\text{Pb}(\text{Mg}_{1/3}\text{Nb}_{2/3})\text{O}_3$ – 0.33PbTiO_3 single crystals. *J Appl Phys.* 2001; 90(7):3471.
78. H.C. Materials Corporation. <www.hcmat.com>
79. Chen Y, Lam KH, Zhou D, Cheng WF, Dai JY, Luo HS, Chan HL. High frequency PMN–PT single crystal focusing transducer fabricated by a mechanical dimpling technique. *Ultrasonics.* 2013; 53(2):345–9. [PubMed: 22944074]

80. Qiu W, Chen Y, Li X, Yu Y, Cheng WF, Tsang FK, Zhou Q, Shung KK, Dai J, Sun L. An open system for intravascular ultrasound imaging. *IEEE Trans Ultrason Ferroelectr Freq Contr.* Oct; 2012 59(10):2201–9.
81. Zhou Q, Xu X, Gottlieb EJ, Sun L, Cannata JM, Ameri H, Humayun MS, Han P, Shung KK. PMN–PT single crystal, high–frequency ultrasonic needle transducers for pulsed–wave Doppler application. *IEEE Trans Ultrason Ferroelect Freq Contr.* 2007; 54(3):668–75.
82. Lam KH, Chan HLW. Piezoelectric cement–based 1–3 composites. *Appl Phys A– Mater.* 2005; 81(7):1451–4.
83. Akdogan EK, Allahverdi M, Safari A. Piezoelectric composites for sensor and actuator applications. *IEEE Trans Ultrason Ferroelect Freq Contr.* 2005; 52(5):746–75.
84. Lam KH, Lo CY, Chan HLW. Frequency response of magnetoelectric 1–3–type composites. *J Appl Phys.* 2010; 107:093901.
85. Zhou D, Cheung KF, Lam KH, Chen Y, Chiu YC, Dai JY, Chan HLW, Luo HS. Broad–band and high–temperature ultrasonic transducer fabricated using aPb(In_{1/2}Nb_{1/2})–Pb(Mg_{1/3}Nb_{2/3})–PbTiO₃ singlecrystal/epoxy 1–3 composite. *Rev Sci Instrum.* 2011; 82(5):055110. [PubMed: 21639541]
86. Zhou D, Lam KH, Chen Y, Zhang Q, Chiu YC, Luo H, Dai J, Chan HLW. Lead–free piezoelectric single crystal based 1–3 composites for ultrasonic transducer applications. *Senor Actuat A–Phys.* 2012; 182:95–100.
87. Lam KH, Guo MS, Lin DM, Kwok KW, Chan HLW. Lead–free piezoelectric BNKLT 1–3 composites. *J Mater Sci.* 2008; 43:1677–80.
88. Sun P, Wang G, Wu D, Zhu B, Hu C, Liu C, Djuth FT, Zhou Q, Shung KK. High frequency PMN–PT 1–3 composite transducer for ultrasonic imaging application. *Ferroelectrics.* 2010; 408(01): 120–8. [PubMed: 21869845]
89. Ritter TA, ShROUT TR, Tutwiler R, Shung KK. A 30–MHz piezo–composite ultrasound array for medical imaging applications. *IEEE Trans Ultrason Ferroelect Freq Contr.* 2002; 49(2):217–30.
90. Lau ST, Li H, Wong KS, Zhou QF, Shung KK. Multiple matching scheme for broadband 0.72Pb(Mg_{1/3}Nb_{2/3})O₃–0.28PbTiO₃ single crystal phased–array transducer. *J Appl Phys.* 2009; 105(9):094908.
91. Chen R, Wu J, Lam KH, Yao L, Zhou QF, Yian J, Han P, Shung KK. Thermal–independent properties of PIN–PMN–PT single–crystal linear–array ultrasonic transducers. *IEEE Trans UltrasonFerroelectFreqContr.* 2012; 59(12):2777–84.
92. www.philips.com/purewave
93. Annema JT, Veselic M, Rabe KF. EUS–guided FNA of centrally located lung tumours following a non–diagnostic bronchoscopy. *Lung Cancer.* 2005; 48(3):357–61. [PubMed: 15893004]
94. Tran QNH, Urayama S, Meyers FJ. Endoscopic ultrasound–guided celiac plexus neurolysis for pancreatic cancer pain: a single–institution experience and review of the literature. *J Support Oncol.* 2006; 4:460–4. [PubMed: 17080734]
95. Savakus HP, Klicker KA, Newnham RE. PZT–epoxy piezoelectric transducers: a simplified fabrication procedure. *Mater Res Bull.* 1981; 16(6):677–80.
96. Zhou D, Cheung KF, Chen Y, Lau ST, Shung KK, Luo HS, Dai JY, Chan HLW. Fabrication and performance of endoscopic ultrasound radial arrays based on PMN–PT single crystal/epoxy 1–3 composite. *IEEE Trans Ultrason Ferroelect Freq Contr.* 2011; 58(2):477–84.
97. Silverman RH, Cannata J, Shung KK, Gal O, Patel M, Lloyd HO, Feleppa EJ, Coleman DJ. 75 MHz ultrasound biomicroscopy of anterior segment of eye. *Ultrason Imaging.* 2006; 28(3):179–88. [PubMed: 17147058]
98. Maresca D, Renaud G, van Soest G, Li X, Zhou Q, Shung KK, de Jong N, van der Steen AF. Contrast–enhanced intravascular ultrasound pulse sequences for bandwidth–limited transducers. *Ultrasound Med Biol.* 2013; 39(4):706–13. [PubMed: 23384459]
99. Vogt M, Ermert H. Limited–angle spatial compound imaging of skin with high–frequency ultrasound (20 MHz). *IEEE Trans Ultrason Ferroelectr Freq Control.* 2008; 55(9):1975–83. [PubMed: 18986893]

100. Dyson M, Moodley S, Verjee L, Verling W, Weinmann J, Wilson P. Wound healing assessment using 20 MHz ultrasound and photography. *Skin Res Technol.* 2003; 9(2):116–21. [PubMed: 12709129]
101. Qiu W, Yu Y, Tsang FK, Zheng H, Sun L. A novel modulated excitation imaging system for micro ultrasound. *IEEE Trans Biomed Eng.* 2013; 60(7):1884–90. [PubMed: 23380848]
102. Zhou Q, Xu X, Gottlieb EJ, Sun L, Cannata JM, Ameri H, Humayun MS, Han P, Shung KK. PMN–PT single crystal, high–frequency ultrasonic needle transducers for pulsed–wave Doppler application. *IEEE Trans Ultrason Ferroelectr Freq Contr.* 2007; 54(3):668–75.
103. Qiu W, Yu Y, Tsang F, Sun L. An FPGA–based open platform for ultrasound biomicroscopy. *IEEE Trans Ultrason Ferroelectr Freq Contr.* 2012; 59(7):1432–42.
104. Chen R, Paeng DG, Lam KH, Zhou Q, Shung KK, Matsuoka N, Humayun MS. In vivo sonothrombolysis of ear marginal vein of rabbits monitored with high–frequency ultrasound needle transducer. *J Med Biol Eng.* 2012; 33(1):103–10. [PubMed: 25356073]
105. Sun L, Xu C, Richard WD, Feng C, Johnson JA, Shung KK. A high–frame rate duplex ultrasound biomicroscopy for small animal imaging In vivo. *IEEE Trans Biomed Eng.* 2008; 55(8):2039–49. [PubMed: 18632366]
106. Yang JM, Favazza C, Chen R, Yao J, Cai X, Maslov K, Zhou Q, Shung KK, Wang LV. Simultaneous functional photoacoustic and ultrasonic endoscopy of internal organs in vivo. *Nature Medicine.* 2012; 18:1297–1302.
107. Lam KH, Hsu HS, Li Y, Lee C, Lin A, Zhou Q, Kim ES, Shung KK. Ultrahigh frequency lensless ultrasonic transducers for acoustic tweezers application. *Biotechnol Bioeng.* 2013; 110(3):881–6. [PubMed: 23042219]
108. Lam KH, Li Y, Lee C, Zhou Q, Shung KK. Ultrahigh frequency ultrasound microbeam for biomedical applications. *Proc IEEE Ultrason Symp.* 2012:1994–7.
109. Hwang JY, Lee NS, Lee C, Lam KH, Kim HH, Woo J, Lin MY, Kislner K, Choi H, Zhou Q, Chow RH, Shung KK. Investigating contactless high frequency ultrasound microbeam stimulation for determination of invasion potential of breast cancer cells. *Biotechnol Bioeng.* 2013; 110(10): 2697–705. [PubMed: 23568761]
110. Meng L, Cai F, Jin Q, Niu L, Jiang C, Wang Z, Wu J, Zheng H. Acoustic aligning and trapping of microbubbles in an enclosed PDMS microfluidic device. *Sensor Actuat B–Chem.* 2011; 160:1599–605.
111. Meng L, Cai F, Chen J, Niu L, Li Y, Wu J, Zheng H. Precise and programmable manipulation of microbubbles by two–dimensional standing surface acoustic waves. *Appl Phys Lett.* 2012; 100:173701.

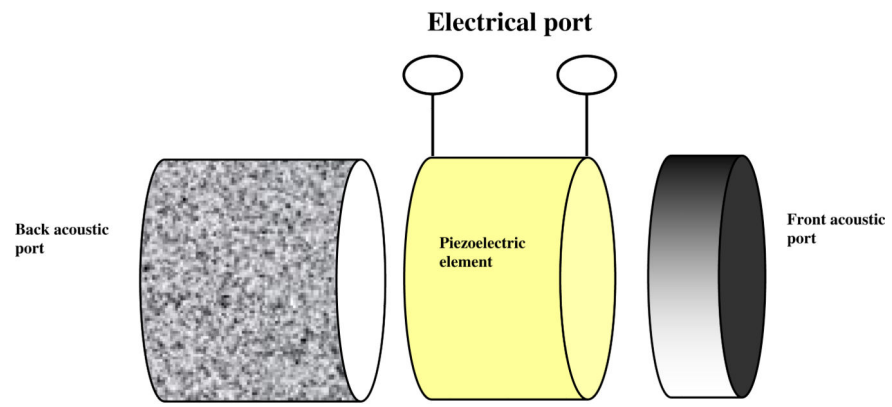


Fig. 1.
A three-port network of the transducer [1].

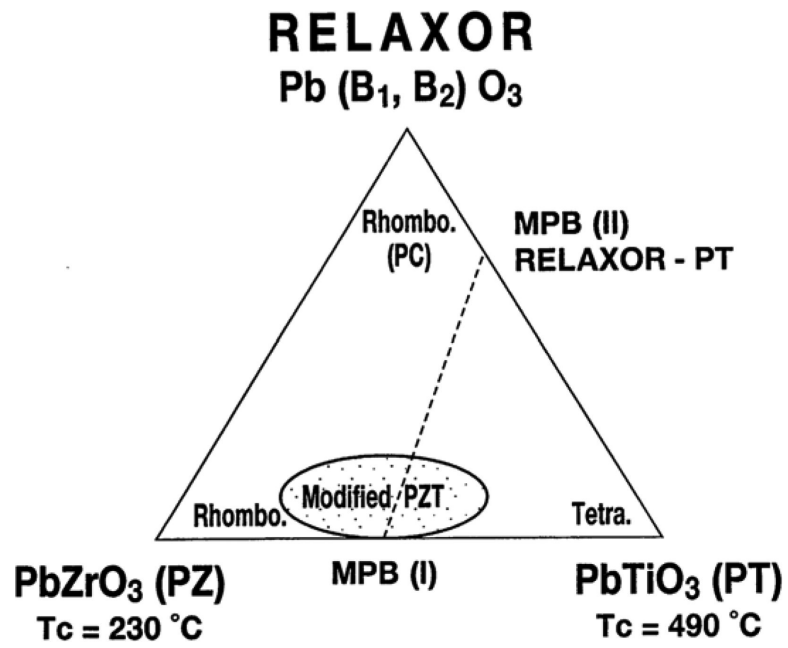


Fig. 2.
Ternary diagram of MPB (I) in PZT and MPB (II) in relaxor-PT systems [46].

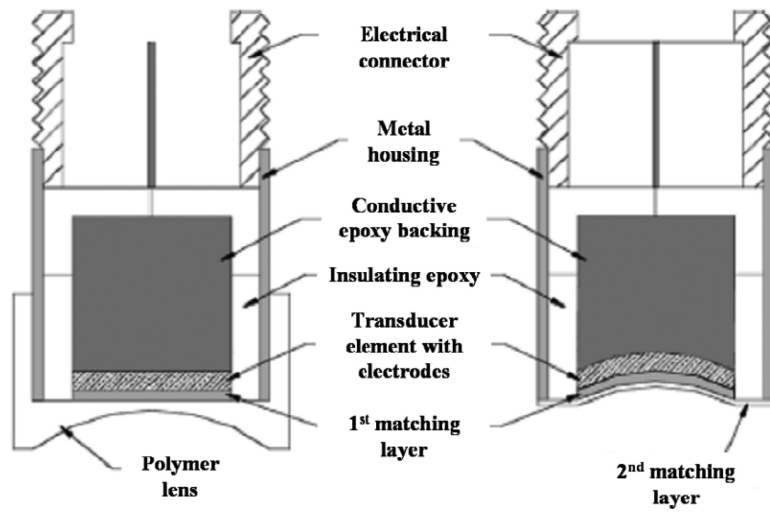


Fig. 3. Design cross sections of the lens-focused (a) and press-focused (b) single-element piston transducers [8].

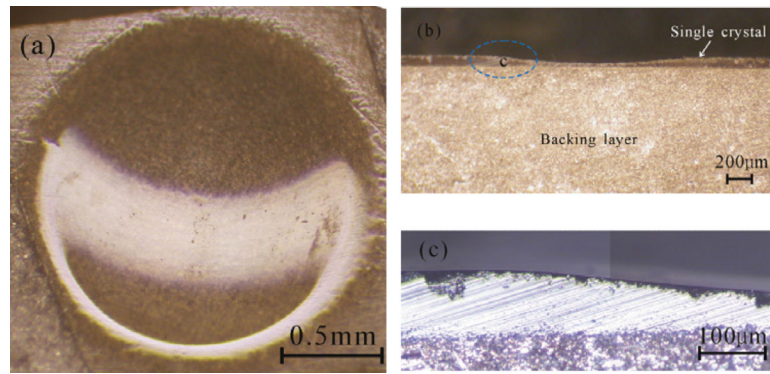


Fig 4. Photographs of (a) top view, (b) cross section view, and (c) a magnified cross section view of the dimpled PMN – PT single crystal with a backing layer [73].

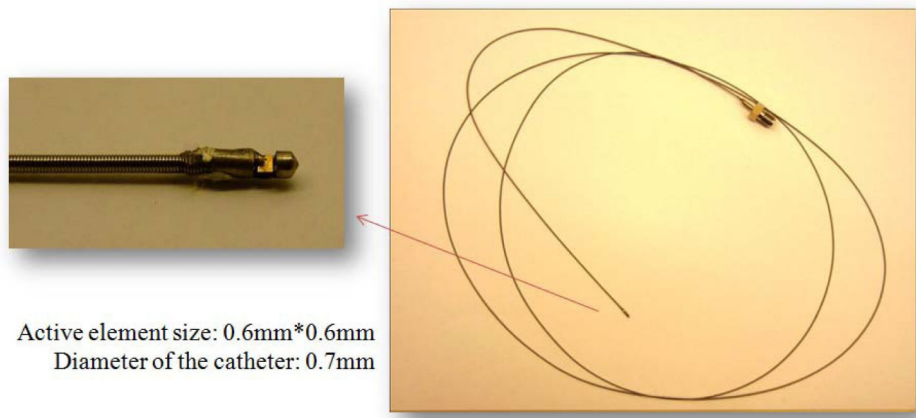


Fig. 5. Side-view of miniature plane transducer designed for intravascular imaging application [74].

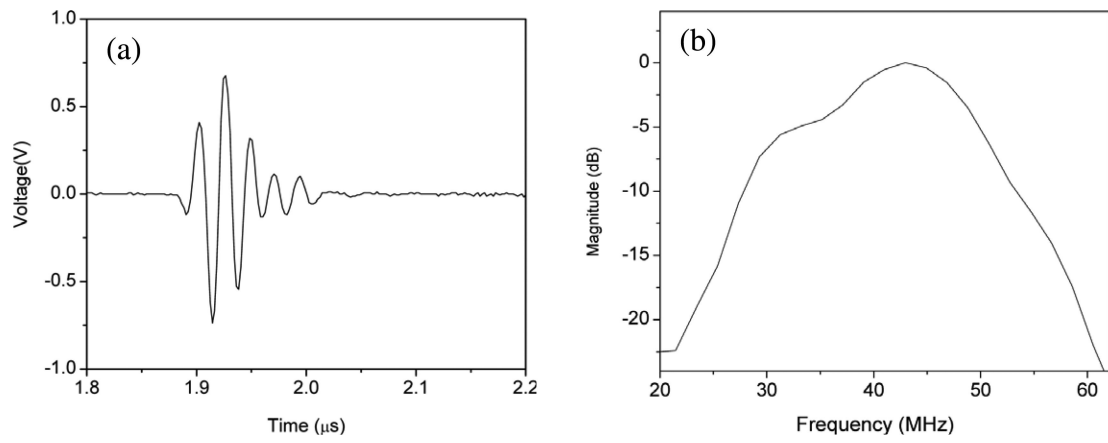


Fig. 6. (a) Measured pulse-echo waveform and (b) frequency spectrum for the 44-MHz PMN-PT needle transducer [75].

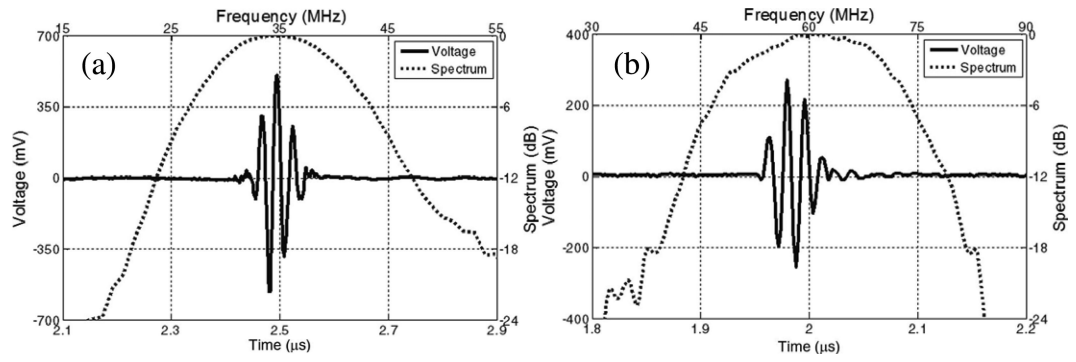


Fig. 7. Measured pulse-echo waveform and spectrum for the (a) 35 MHz and (b) 60 MHz PIN-PMN-PT piston transducer [67].

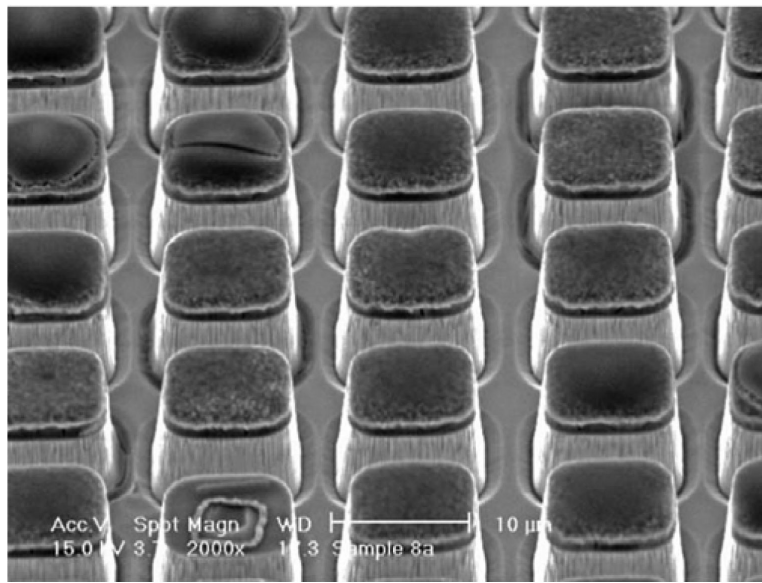


Fig. 8.
SEM micrograph of the etched PMN-PT single crystal [82].

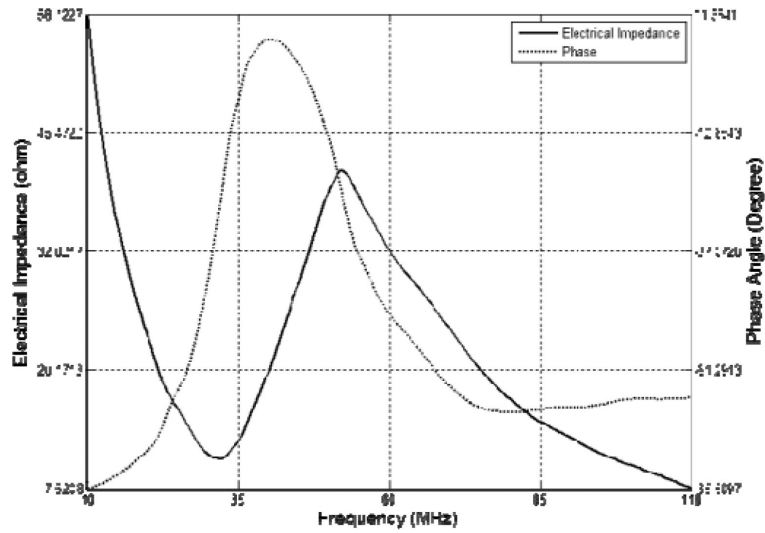


Fig. 9. Measured electrical impedance/phase for the PMN-PT single crystal/epoxy 1-3 composite transducer [82].

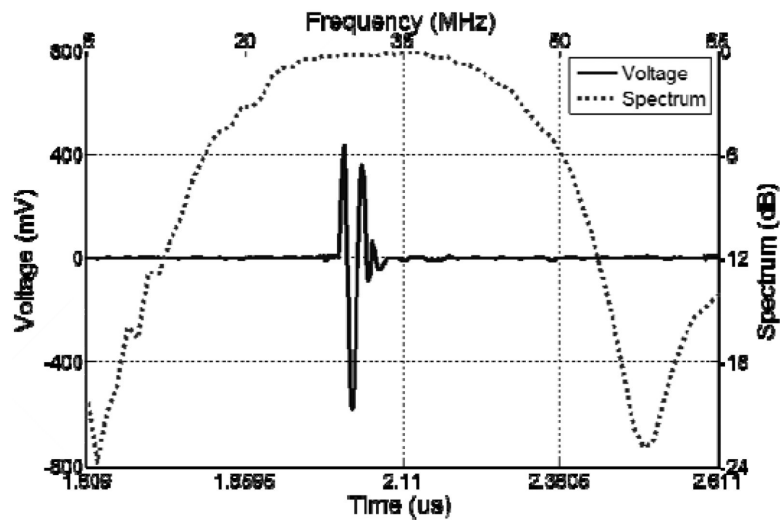


Fig. 10. Measured pulse-echo impulse response and frequency spectrum of the PMN-PT single crystal/epoxy 1-3 composite transducer [82].

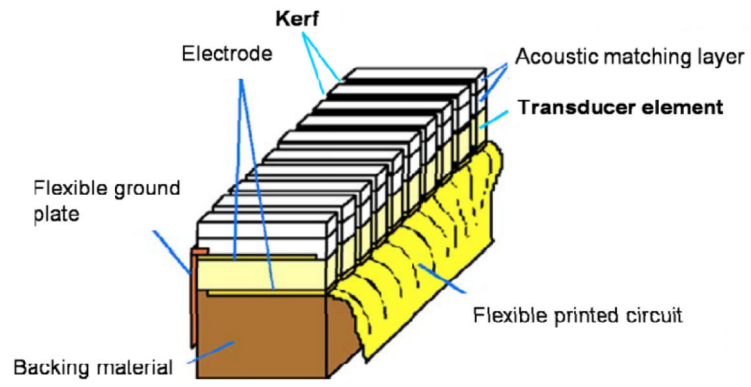


Fig. 11.
Schematic diagram of a linear array transducer [84].

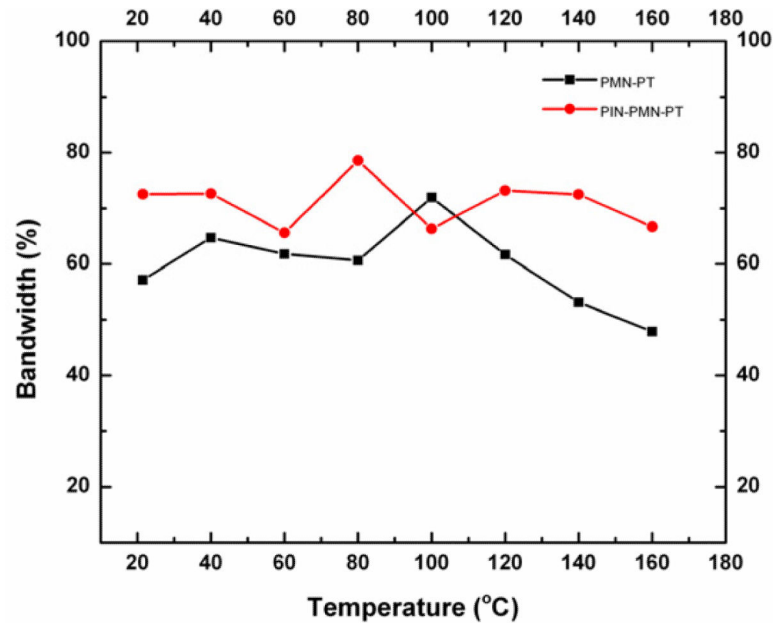


Fig. 12. Comparison of -6 dB bandwidth of PMN-PT and PIN-PMN-PT single

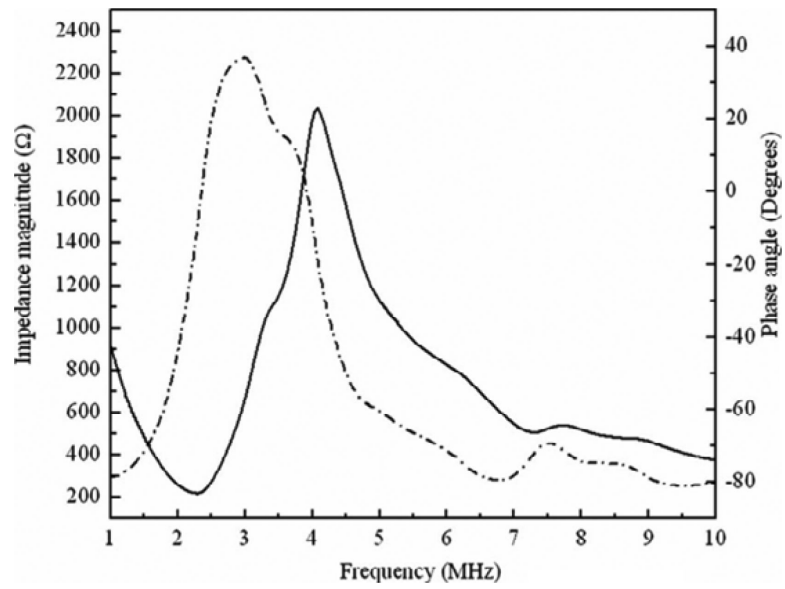


Fig. 13. Measured electrical impedance/phase for the PMN-PT single crystal array element. The solid and dotted lines represent the impedance and phase, respectively [84].

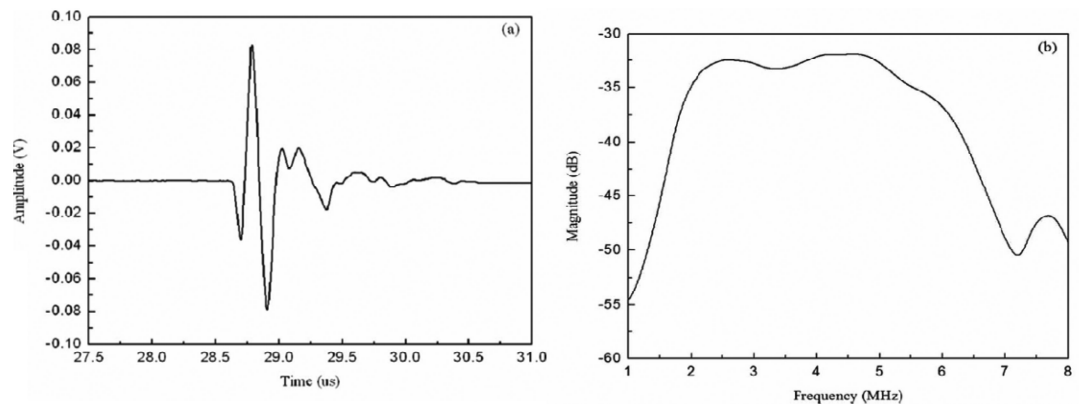


Fig. 14. (a) Measured pulse-echo impulse response and (b) frequency spectrum of the PMN-PT single crystal array element [84].

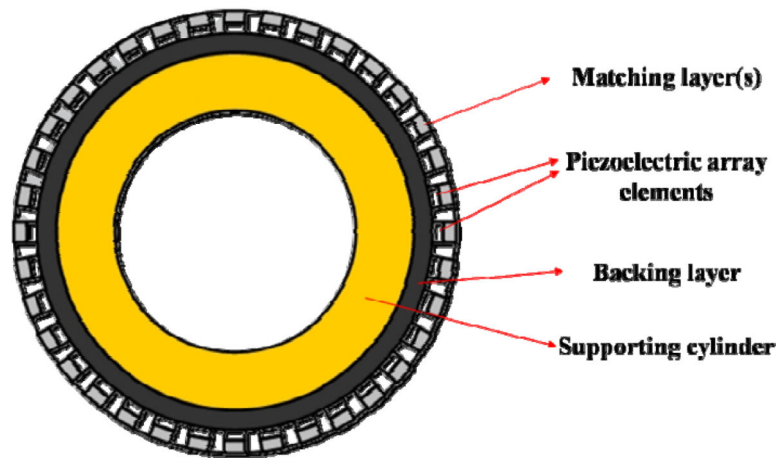


Fig. 15.
Schematic cross section view of a radial array transducer [89].

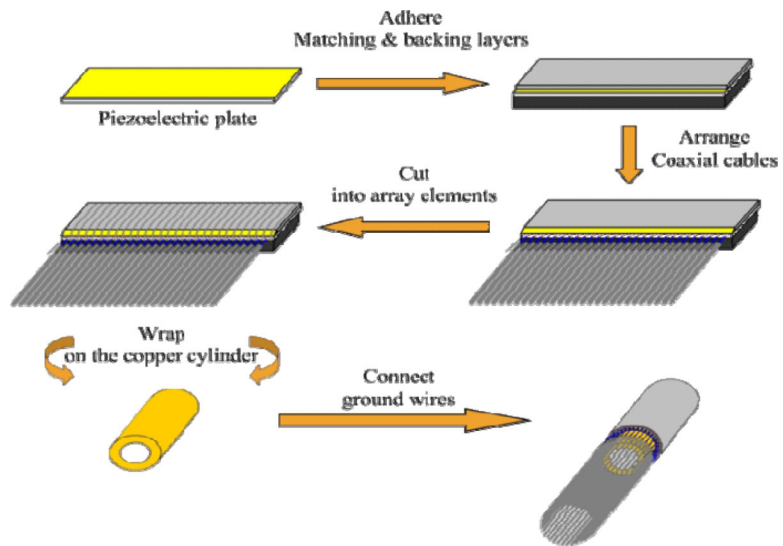


Fig. 16. Fabrication procedures of a PMN-PT/epoxy 1-3 composite radial array transducer [89].

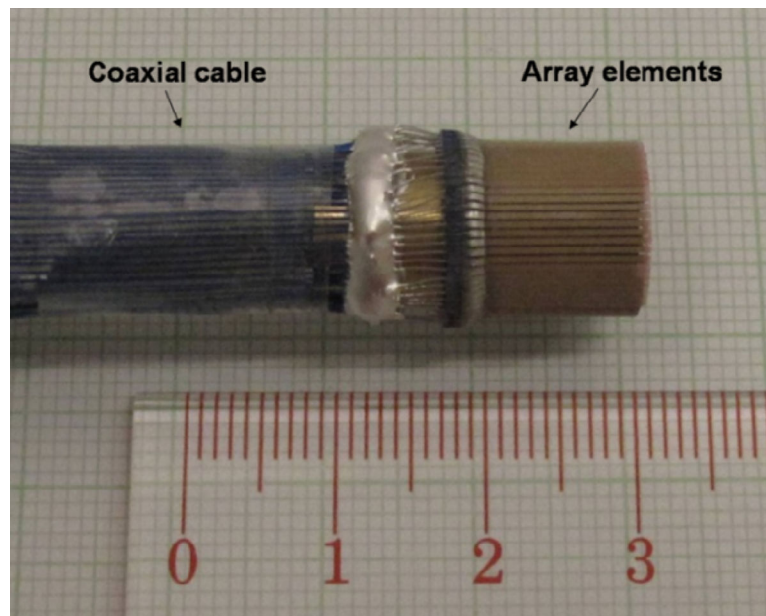


Fig. 17. Photograph of a PMN-PT/epoxy 1-3 composite radial array transducer [89].

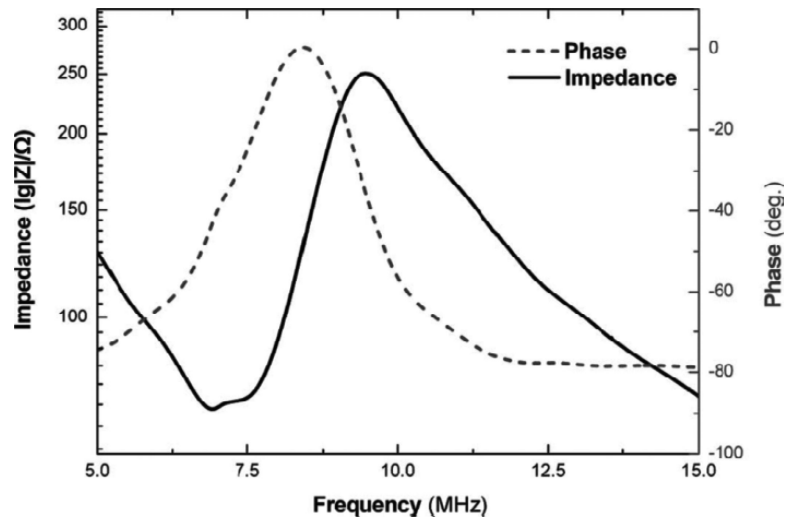


Fig. 18. Measured electrical impedance magnitude (solid line) and phase angle (dashed line) for a representative composite array element [89].

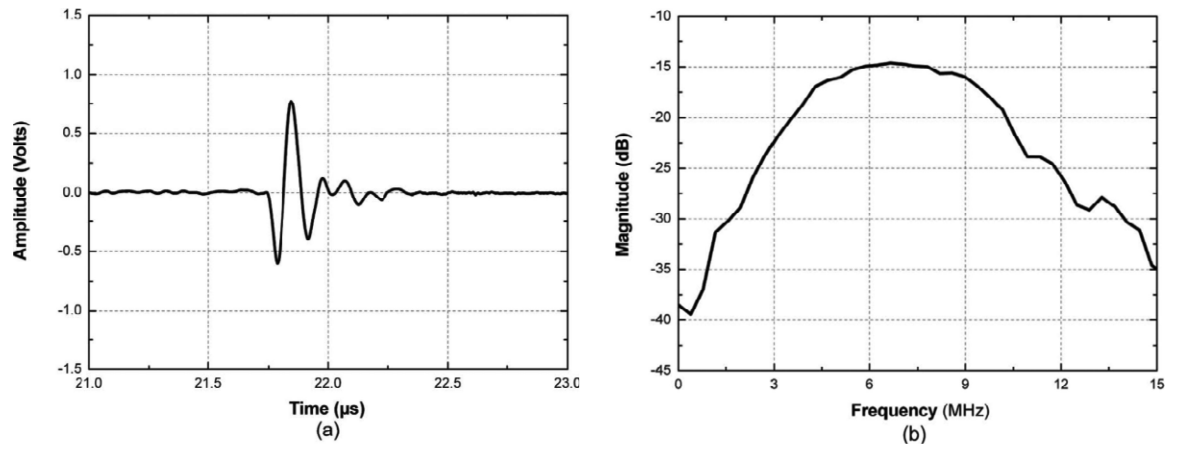


Fig. 19. Measured pulse-echo response for a representative composite array element [89].

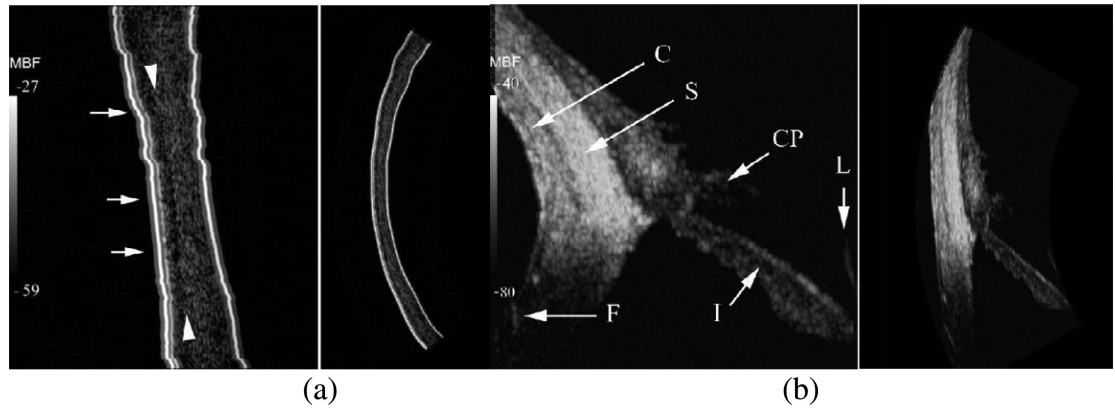


Fig. 20.

(a) LASIK-treated cornea six years post-treatment imaged at 75 MHz. Small arrows indicate various discontinuities in Bowman's layer, at the interface of the 50 μm thick epithelium and the underlying stroma. The stroma anterior to the ablation interface is approximately 2–3 dB lower in mean backscatter than the posterior residual stroma. (b)

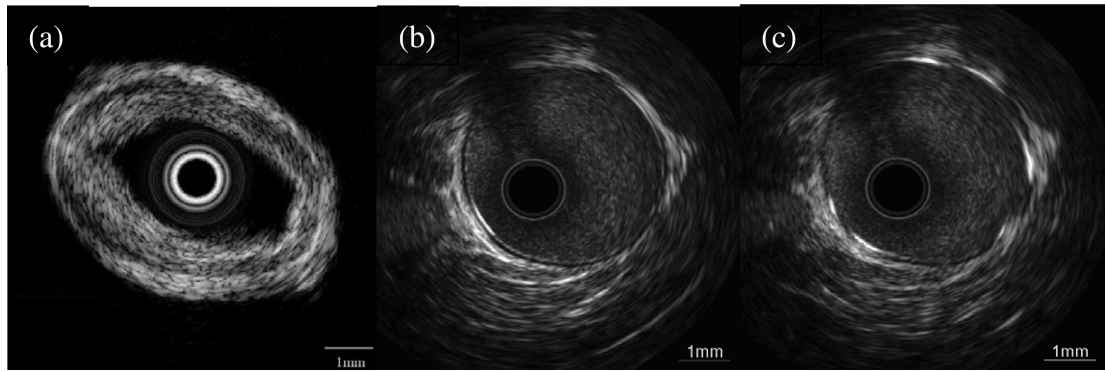


Fig. 21.

(a) *In vitro* imaging of human coronary artery acquired by a 32-MHz PMN-PT single crystal catheter. (b) Intravascular image of a porcine vessel taken with a 60-MHz 1-3 composite based transducer. (c) Intravascular image of a porcine vessel with stent taken with a 60-MHz 1-3 composite based transducer [91].

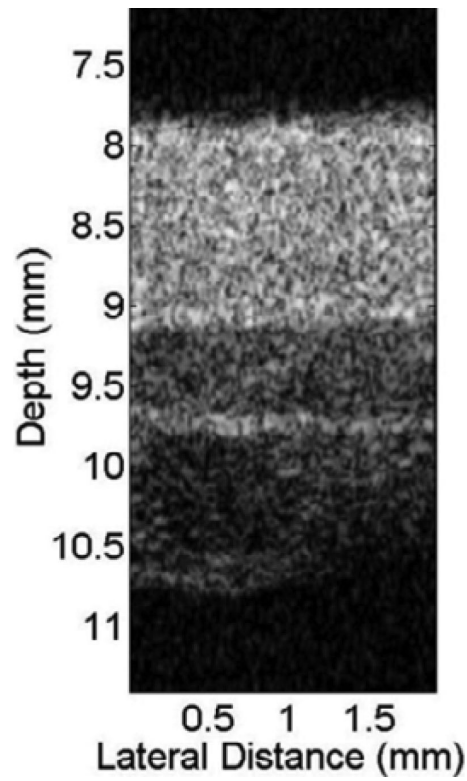


Fig. 22.
In vivo image of the dorsal skin of a human hand by high resolution single crystal transducer [94].

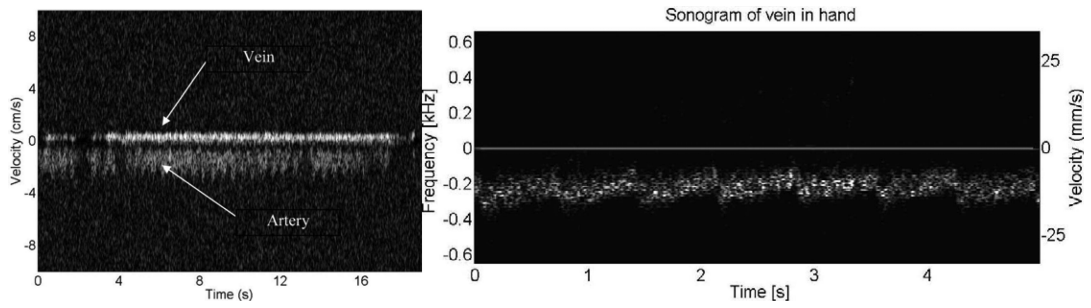


Fig. 23.

(a) Retinal arterial blood flow of a New England Cottontail rabbit Doppler frequency spectrum measured *in vivo* [95]. (b) Blood flow of a vein in the back of a human hand *in vivo* [96].

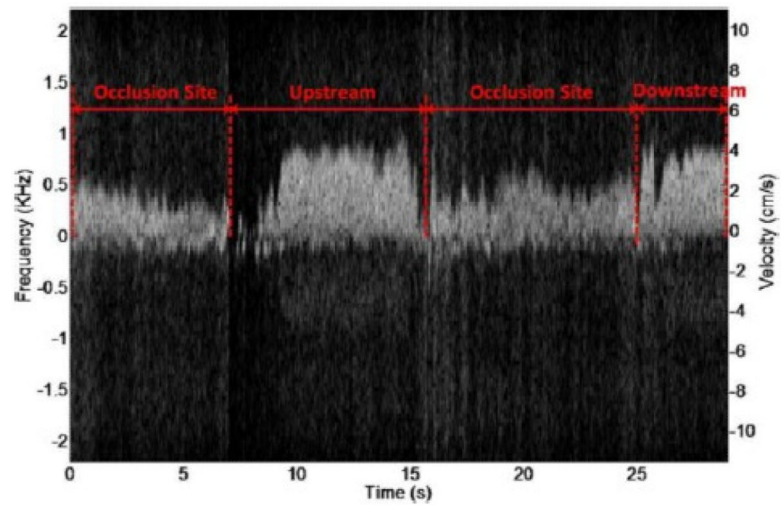


Fig. 24. Doppler spectrogram of the rabbit ear marginal vein after opening of the occlusion by high-intensity US insonation right after microbubble injection [97].

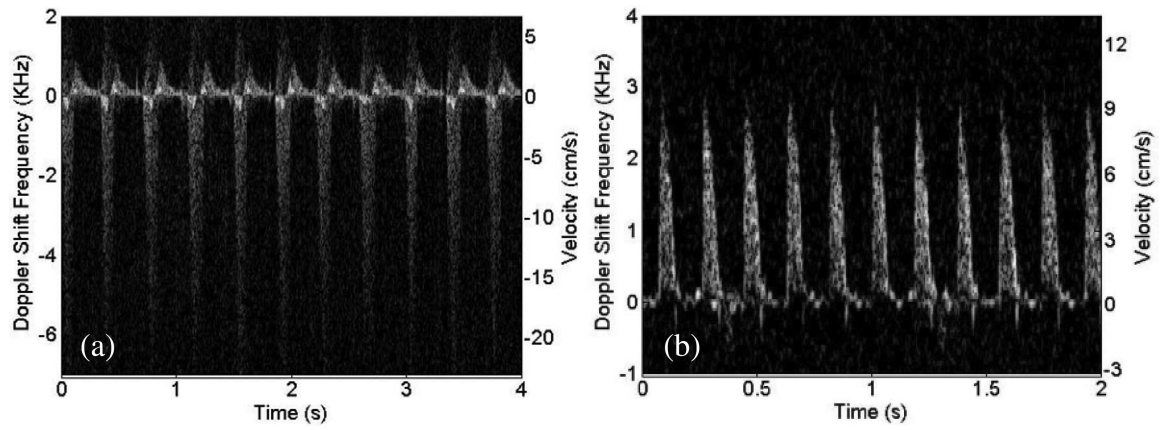


Fig. 25.
(a) Ventricular Doppler waveform and (b) aortic Doppler waveform of the mouse heart acquired with a 75-MHz LN single crystal based transducer [98].

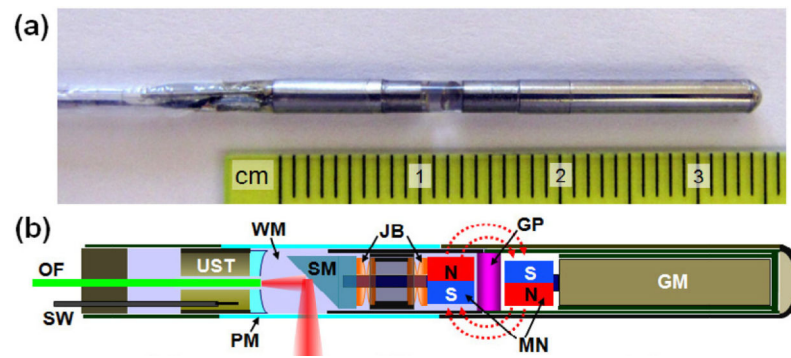


Fig. 26.

(a) Photo of the integrated mini-probe's rigid distal end. (b) Schematic of the mini-probe. GM, geared micromotor; GP, glass partition; JB, jewel bearings; MN, magnets; OF, optical fiber; PM, plastic membrane (imaging window); SM, scanning mirror; SW, signal wire; UST, ultrasonic transducer; WM, water medium [99].

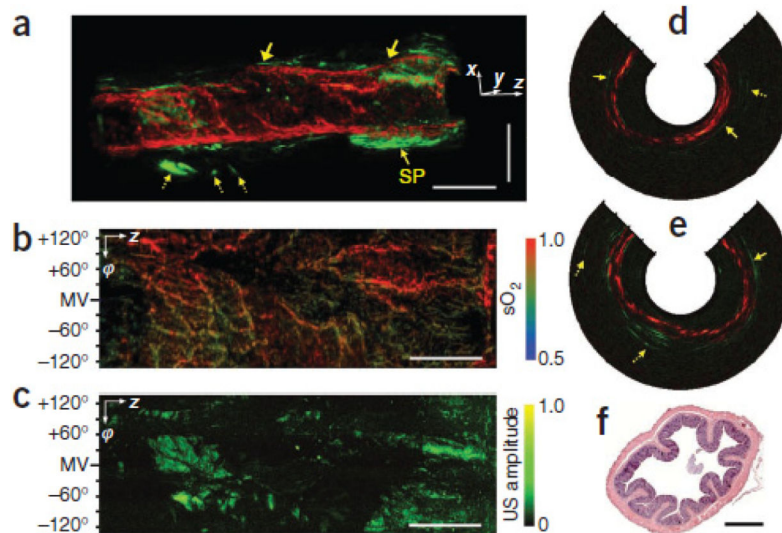


Fig. 27. Simultaneous, co-registered, colonoscopic pseudo color images of a rat colon acquired *in vivo*. (a) 3D rendered photoacoustic-ultrasonic structural image. (b) Photoacoustic image showing the SO_2 levels of the imaged structures in a (views from the inside of the colon). (c) Corresponding (to b) ultrasonic image showing the echogenicity distribution. (d, e) Photoacoustic-ultrasonic cross-sectional images from the position indicated by the left and right arrows in a, respectively. In (d) and (e), the solid arrows indicate the outer boundary of the colon, and mesenteric tissues are marked with dotted arrows. The hash marks represent 1-mm intervals. (f) A typical histology image (H&E stain) of the colon. Scale bar: 1 mm [99].

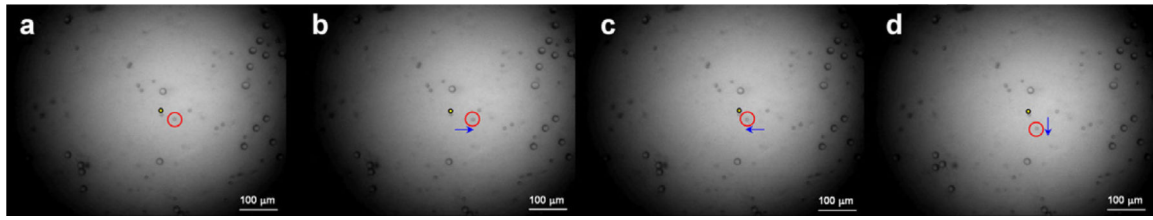


Fig. 28.

Example of microsphere manipulation using the 200-MHz LN transducer. A single 5 μm microsphere was manipulated along the movement of the 200-MHz transducer. A red circle is a trapped microsphere while a yellow dot is given as a reference point to show the location change of the microsphere. (The capturing frame rate was 10 frames/s.) [100]

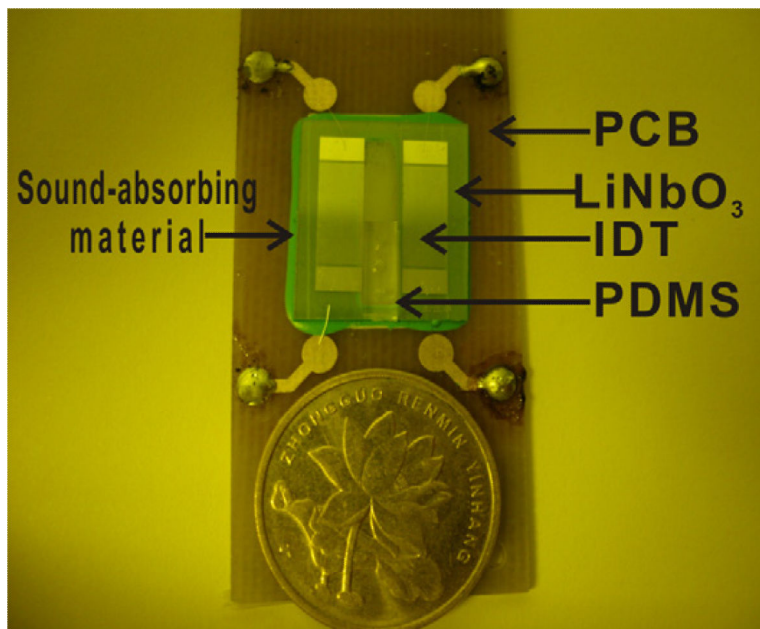


Fig. 29. Photograph of the microfluidic device. LN crystal is used as a substrate to generate ultrasonic wave because of its high coupling coefficient [103].

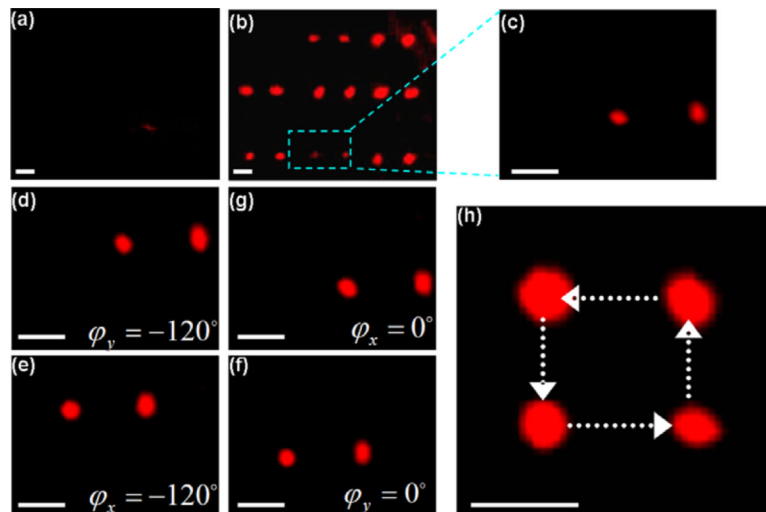


Fig. 30.

The behavior of the MBs in the microfluidic device (a) prior to and (b) after application of ultrasonic wave. (c) The enlarged image of the MB cluster. (d), (f) Transportation of MB cluster along the Y direction. (e), (g) Transportation of MB cluster along the X direction. (h) The composite image shows the trajectory of the MB cluster. The scale bar is $20 \mu\text{m}$ [104].

Table 1

Properties of passive materials used in transducer design.

	Density (kg/m ³)	Velocity (m/s)	Acoustic impedance (MRayl)	Loss (dB/mm)
Matching layer material				
Epo-tek 301 [8]	1150	2650	3.05	9.5 @ 30 MHz
* Alumina-loaded epoxy [9]	1100–1900	2650–2800	3.0–5.5	12–17 @ 30 MHz
* Silver-loaded epoxy [8]	3860	1900	7.30	13.8 @ 30 MHz
Parylene [8]	1180	2200	2.60	N/A
Backing layer material				
E-solder 3022 (centrifuged) [8]	3200	1850	5.92	110 @ 30 MHz
* Tungsten-loaded epoxy [7]	2000–4350	1500–2300	3–10	25–55 @ 36 MHz

* The volume fraction of the loading material is ranged from 5 – 30 %.

Table 2

Material properties of the single crystals used in ultrasonic transducers.

	LN [40, 42]	PMN-PT [59, 71, 72]	PIN-PMN-PT [63, 65]
Properties			
ρ (kg/m ³)	4700	8060	8198
d_{33} (pC/N)	~−49	2820	2742
k_t	0.39	0.58	0.59
k_{33}	0.47	0.94	0.95
e_{33}^s	39	680–800	659
c_p (m/s)	7340	4610	4571
Z_a (MRayl)	34.5	37.1	37.5
T_{rt} (°C)	—	60–95	100–117
T_c (°C)	1140	130	~−200